THESIS FOR THE DEGREE OF LICENTIATE OF ENGINEERING

Electron Microscopy Investigation of Detailed Microstructures of CVD TiAlN and TiN Coatings

Effects of Gas Flow and Substrate on Coating Microstructure

REN QIU

Department of Physics

CHALMERS UNIVERSITY OF TECHNOLOGY

Gothenburg, Sweden 2020

Electron Microscopy Investigation of Detailed Microstructures of CVD TiAlN and TiN Coatings
Effects of Gas Flow and Substrate on Coating Microstructure

REN QIU

© REN QIU, 2020.

Department of Physics
Chalmers University of Technology
SE-412 96 Gothenburg
Sweden
Telephone + 46 (0)31 772 10 00

Chalmers Reproservice
Gothenburg, Sweden 2020

To my family

Electron Microscopy Investigation of Detailed Microstructures of CVD TiAlN and TiN Coatings - Effects of Gas Flow and Substrate on Coating Microstructure

Ren Qiu
Department of Physics
Chalmers University of Technology

Abstract

This thesis contains studies of topics of relevance to increase the understanding of TiN and TiAlN coatings synthesized by chemical vapour deposition (CVD) and low pressure CVD (LPCVD), respectively. This work contains two parts: (i) nanolamella LPCVD TiAlN coatings that were found to show a spatial variation of their chemical composition and microstructure, which was influenced by the gas flow speed of reactants; (ii) microstructure of CVD TiN coating deposited onto a CoCrFeNi multi-principal element alloy (MPEA)substrate.

Depositing homogeneous TiAlN coatings on cutting tool inserts to achieve extraordinary mechanical performance and good chemical stability remains a challenging task. In this work, the detailed microstructure of high-Al cubic $Ti_{1-x}Al_xN$ coatings (average $x = 0.8$) made by LPCVD was studied by state-of-the-art electron microscopy. A periodic structure with Ti-rich and Al-rich nanolamellae was found. Ti enrichment appears at high gas flow rate, which is suggested to be due to the increase of mass transport of certain reactants. However, the higher mass transport does not influence the Al-deposition much, as it is mainly limited by surface kinetics. A co-growth of h-AlN and TiAlN was investigated by electron microscopy, which showed that the h-AlN prefers to form on the Ti-rich cubic phase following a specific crystallographic orientation relationship: $[110]_{cub}$ // $[2\bar{1}\bar{1}0]_{hex}$, and $(001)_{cub}$ // $(0001)_{hex}$. This can be explained by a low interface energy between the h-AlN and Ti-rich cubic phase according to density functional theory (DFT) modelling. The microstructural inhomogeneity of TiAlN coatings can therefore be explained by the co-growth of the h-AlN phase with the Ti-rich cubic phase, which is caused by a fast gas flow.

An electron microscopy study was done on the microstructure of TiN coatings grown on a CoCrFeNi MPEA substrate. The MPEA shows a good capability of serving as a CVD substrate. No severe etching of the substrate was found, and the growth of TiN was not disturbed by the substrate material. However, grain boundary diffusion of Cr into the TiN coating was revealed by analytical electron microscopy.

Keywords: CVD, TEM, SEM, EBSD, coating growth

Acknowledgements

It gives me great pleasure to express my appreciation to the people who have supported me in the first two years of my PhD study. My deepest gratitude goes to the Division of Microstructure Physics at the Department of Physics at Chalmers University of Technology. Here, I would like to first thank my supervisor Prof. Mats Halvarsson for his support on guiding the PhD project. I am grateful for your being always open-minded and with great patience when we have different opinions. I want to sincerely thank Dr. Olof Bäcke for his kind support on the project ideas and experimental work. I want to say grateful thanks to Prof. Hans-Olof Andrén for his valuable help on scientific discussions and paper writing. I would also like to thank Dr. Anand. H. S. Iyer, and Dr. Mohammad Sattari for their help on the experiments. I want to thank Dr. Lunjie Zeng, and Dr. Stefan Gustafsson, for their valuable help regarding electron microscopy. I want to thank Ola Löfgren for always giving computer support. I also want to thank Andrea Fazi for being a nice and warm-hearted officemate. My thanks go to all people from the Division of Microstructure Physics, the Eva Olsson Group, and Chalmers Materials Analysis Laboratory (CMAL) for maintaining a peaceful working environment.

My sincere thanks go to Axel Forslund, Prof. Henrik Larsson, and Prof. Andrei Ruban, from the Royal Institute of Technology, for their essential contribution with DFT simulations. My thanks also go to Katalin Böör, and Prof. Mats Boman, from Uppsala University, for their close collaboration. I would like to thank Drs. Dirk Stiens, Wiebke Janssen, Thorsten Manns, and Johannes Kümmel, from Walter AG in Germany, for their kind and valuable help on the project. I want to thank Dr. Erik Lindahl, and Dr. Linus von Fieandt, from Sandvik Coromant, Sweden, for the discussions.

Finally, I sincerely thank my beloved family for always standing by my side. My love to you all.

List of Publications

This thesis is mainly based on the work presented in the following two appended papers. In the text, they are referred to by roman numbers.

Paper I

Ren Qiu, Axel Forslund, Olof Bäcke, Mohammad Sattari, Anand. H. S. Iyer, Wiebke Janssen, Thorsten Manns, Johannes Kümmel, Andrei Ruban, Dirk Stiens, Hans-Olof Andrén, and Mats Halvarsson.

'Effects of gas flow on detailed microstructure inhomogeneities in LPCVD TiAlN nanolamella coatings.'

Materialia 9 (2020) 100546.

Paper II

Katalin Böör, **Ren Qiu**, Axel Forslund, Olof Bäcke, Henrik Larsson, Erik Lindahl, Mats Halvarsson, Mats Boman, and Linus von Fieandt.

'Chemical Vapor Deposition of TiN on a CoCrFeNi multi-principal element alloy substrate. '

Under review of ***Surface and Coatings Technology***.

Statement of Contribution

My contribution to the papers listed above:

In paper I: As the principal author, I performed the sample preparation, microscopy experiments, result analysis, and wrote the paper with other co-authors under the supervision of my advisors.

In paper II: As the second author, I prepared the samples for microscopy study, performed microscopy experiments, result analysis, and wrote the experimental methods and results of electron microscopy and the corresponding discussions in the paper under the supervision of my advisors.

Preface

The work presented in this thesis was performed at the Division of Microstructure Physics, Department of Physics, Chalmers University of Technology, Sweden, collaborating with Uppsala University, the Royal Institute of Technology, Sandvik Coromant and Walter AG, during the period 2017-2020. The work was performed under the supervision of Prof. Mats Halvarsson. This research was part of the program *CVD 2.0* funded by the Swedish Foundation for Strategic Research, contract RMA15-0048, and Sandvik AB.

Gothenburg, 26th March 2020

Ren Qiu

List of Acronyms

AE	Auger Electrons
APCVD	Atmospheric Pressure Chemical Vapour Deposition
BF	Bright Field
CFD	Computational Fluid Dynamics
CVD	Chemical Vapour Deposition
DF	Dark Field
DFT	Density Functional Theory
EBSD	Electron Backscattered Diffraction
EELS	Electron Energy Loss Spectroscopy
EFTEM	Energy Filtered Transmission Electron Microscopy
FCC	Face Centered Cubic
FEG	Field Emission Gun
FFT	Fast Fourier Transform
FIB	Focused Ion Beam
GB	Grain Boundary
HAADF	High Angle Annular Dark Field
HRSTEM	High Resolution Scanning Transmission Electron Microscopy
LPCVD	Low Pressure Chemical Vapour Deposition
MPEA	Multi-Principal Element Alloy
PVD	Physical Vapour Deposition
SAED	Selected Area Electron Diffraction
SEM	Scanning Electron Microscopy
STEM	Scanning Transmission Electron Microscopy
TEM	Transmission Electron Microscopy
TKD	Transmission Kikuchi Diffraction
XEDS	X-Ray Energy Dispersive Spectrometry
XRD	X-Ray Diffraction

Table of Contents

1 Introduction 1

1.1 Background of wear resistant coatings 1

1.2 Analytical electron microscopy 1

1.3 Scope of the thesis 2

2 Chemical vapour deposition 3

2.1 Basic principles 3

2.2 CVD coating growth rate 4

2.3 Low pressure chemical vapour deposition 5

3 Hard coating materials 7

3.1 Titanium nitride 7

3.2 Titanium aluminium nitride 8

3.3 Aluminium nitride 10

4 Experimental procedure 11

4.1 X-ray diffraction 11

4.2 Scanning electron microscopy 12

4.3 Transmission electron microscopy 15

4.3.1 Instrument configurations 15

4.3.2 TEM mode 18

4.3.3 STEM mode 19

4.3.4 X-ray energy dispersive spectrometry 20

4.3.5 Electron energy loss spectroscopy 22

4.3.6 STEM probe size and imaging resolution 23

4.3.7 Beam broadening and spectrometry/spectroscopy resolution 24

4.4 Focused ion beam technique 26

4.5 Electron backscattered diffraction and transmission Kikuchi diffraction 27

4.6 Modelling consideration 29

4.6.1 Computational fluid dynamics 29

4.6.2 Density functional theory 29

4.6.3 Thermodynamic modelling 30

5 **Results and Discussion** 31
5.1 Co-growth of h-AlN and TiAlN phases 31
5.2 Gas flow effect on Ti and Al deposition 31
5.3 Microstructural inhomogeneity in TiAlN coatings 32
5.4 Diffusion of Cr from a CoCrFeNi substrate through TiN grain boundaries 32
6 **Future work** 35
6.1 Quantification of chemical compositions of TiAlN nanolamellae 35
6.2 Rotation speeds and nanolamella periodicities 35
7 **References** 37

1 Introduction

This thesis is mainly concerned with topics of relevance for developing the understanding of the microstructure of TiN and TiAlN hard coatings produced by chemical vapour deposition (CVD). These coatings have been widely used to increase the wear resistance of cemented carbide tools in the cutting tool industry. However, much research remains to fully understand the growth mechanism and microstructural details of these CVD coatings. This study mainly consists of two topics: (i) the gas flow effect on the microstructural inhomogeneity of TiAlN coatings; (ii) the microstructure of TiN coatings deposited on a CoCrFeNi multi-principal elemental alloy (MPEA) substrate.

1.1 Background of wear resistant coatings

Depending on the large variety of workpiece materials to be machined and correspondingly different cutting conditions, a wide range of hard materials has been developed since the 1970's to coat cutting tools, usually based on cemented carbides (WC-Co based hard materials) [1]. The extreme conditions during cutting operations include high-temperatures (exceeding 1000 ºC), and high-pressure loads. The extreme machining conditions therefore require superior properties of the hard coating materials, including extraordinary hot hardness (hardness at high temperatures), oxidation resistance, adhesion to the substrate material and chemical stability. The hardness is one of the most essential property that influences the mechanical performance of coatings. Approximate hardness values of typical coating phases are presented in Fig. 1.1. The diamond coating exhibits the highest hardness [2]. However, the application of CVD diamond coating is limited by its inferior adhesion to the cemented carbide substrate, which is caused by the significant residual stress formed during the CVD process [3]. In addition, the wear performance of diamond coatings is influenced by dissolution of carbon from the coating into many workpiece materials (such as steels). Therefore, the most frequently used hard CVD coating materials are Al_2O_3, TiN, TiAlN, and TiCN [4–7].

1.2 Analytical electron microscopy

This research is concerned with microstructural characterization of hard coating materials. Analytical electron microscopy, combining imaging with X-ray energy dispersive spectrometry (XEDS) and electron energy loss spectroscopy (EELS), enables microstructural investigations with high spatial resolution, providing both crystallographic and chemical information. Since

analytical scanning/transmission electron microscopy (STEM/TEM) is a central part of this thesis, details of the techniques and the corresponding applications will be described in the chapters below.

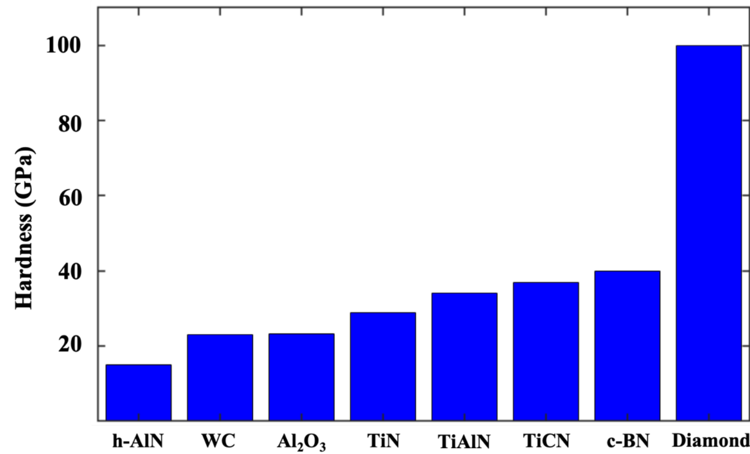

Figure 1.1. Hardness of various coating materials. Values for h-AlN [8,9], WC [10], sapphire (α-Al_2O_3) [11], TiN [12,13], TiAlN [12,13], TiCN [6], c-BN [14], and diamond [2] coatings are shown.

1.3 Scope of the thesis

This thesis is mainly concerned with TiN and TiAlN hard coatings synthesized by CVD. The CVD TiAlN coatings exhibit a noticeable inhomogeneity, which is shown to be influenced by the local gas flow rate of precursor molecules, and influences the cutting performance of the cutting tools. Therefore, correlations between the coating microstructure and the local gas flow rate were studied. In paper I, the focus is on relating the CVD gas flow to the detailed microstructural inhomogeneities of the TiAlN coatings containing a fascinating nanolamella structure. Microstructural inhomogeneities caused by local gas flow variations are described in detail. The co-growth of the hexagonal AlN (h-AlN) phase with the nanolamella TiAlN is further explored by density functional theory (DFT) simulations. CoCrFeNi MPEA show prominent mechanical properties, where future application possibilities could be broadened through coating with hard wear resistant materials. Therefore, the capability of coating CoCrFeNi substrates by CVD at high temperature and corrosive environment needs to be evaluated. In paper II, the microstructure of TiN coatings deposited on a CoCrFeNi MPEA substrate is studied. The etching effect on the substrate and the diffusion of the substrate elements through coating grain boundaries are investigated by analytical STEM.

2 Chemical vapour deposition

2.1 Basic principles

Chemical vapour deposition (CVD) is an important technology for synthesizing wear resistant protective thin films on cutting tools with good adhesion [15–24]. CVD has been intensively used to produce various metals, non-metallic element materials, oxides, nitrides and carbides [25]. In CVD synthesis, gaseous precursors, usually metal halides with reducing agents, react at high temperature to form a solid phase. CVD reactions can happen homogeneously in the gas phase and form particles that fall down onto the substrate, which yields inferior coatings with porosity and poor adhesion to the substrate. Ideally, precursors should react heterogeneously at the substrate surface to form coatings with good qualities. The undesired homogeneous nucleation in CVD can be avoided by heating the coating substrate, and choosing reactant species that exhibit strong chemisorption to the substrate and need thermal activation to react [26]. The growth of CVD coatings is governed by thermodynamics that controls the driving forces of the chemical reactions, and by reaction kinetics that determines the coating growth rate.

Most of the CVD synthesis processes involve endothermic chemical reactions that need energy input to be activated. There are several approaches for activating the reactivity of the gaseous reactants and lowering the reaction temperatures. The activation energy can be lowered by exciting the gaseous precursors with a plasma to create reactive intermediate products, called plasma enhanced CVD (PECVD) [27]. The substrate surface is heated locally by a laser beam to activate the surface reaction in laser assisted CVD (LACVD) [28]. LACVD is also applied to stimulate the gaseous precursors to excited states by illuminating with characteristic light wavelengths, which lowers the decomposition energy of reactant chemicals and thus the deposition reaction temperature. Another approach is thermally activated CVD (TACVD), which is implemented by heating the entire chamber (hot wall CVD), heating the substrate (cold wall CVD), or activating the gas phase through a heating filament (hot filament CVD). The coating samples investigated in this work were prepared in an industrial scale hot wall CVD reactor at Walter AG in Germany, and in an industrial scale reactor at Sandvik Coromant in Sweden.

The kinematic CVD process includes several events happening in sequence (and in parallel) [25,29], as graphically illustrated in Fig. 2.1. The gaseous reactant molecules are transported

towards the substrate to be deposited by the main gas stream in the reactor. The reactant molecules diffuse through a stagnant layer, which is formed by the gas flowing above the substrate surface [25]. The reactant molecules get adsorbed/dissociated on the substrate surface, where the binding strength influences the mobilities of the molecules on the surface. Reactant molecules diffuse on the surface to find sites with steps and kinks that form more stable bonds with the molecules. The surface reaction of reactant molecules forms a deposited solid phase, where byproduct molecules are created. The byproducts get desorbed and diffuse away from the surface through the stagnant layer, and are transported away from the deposited area by the gaseous flow.

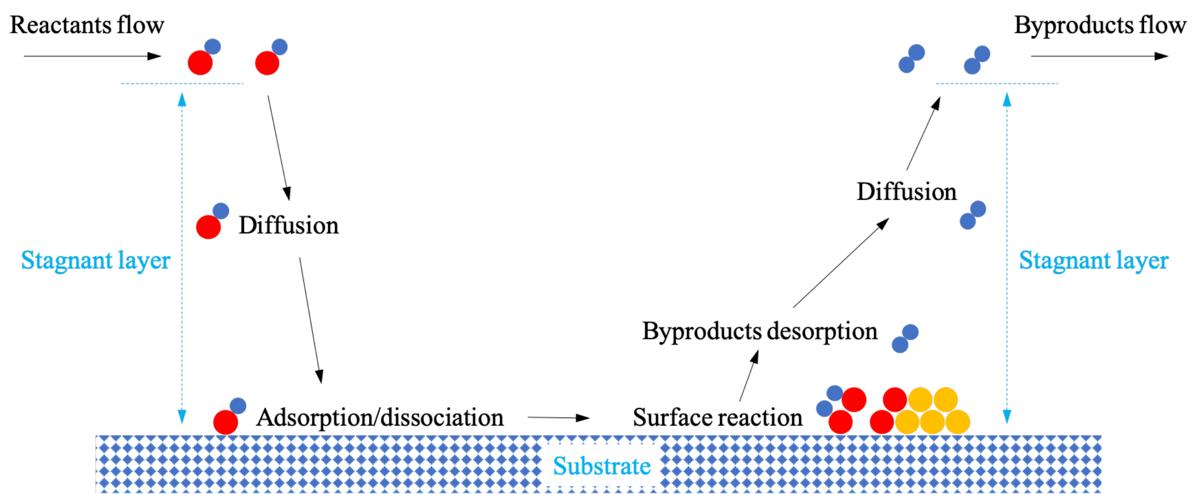

Figure 2.1. Schematics of the sequence of events during a CVD process.

However, stable coating growth is not always obtained due to the complexity of the CVD process. The surface reaction and deposition rates are influenced by several factors, including types of the precursor species, deposition temperature, and mass transport rate. To obtain a stable, predictable coating growth, it is therefore essential to understand the kinetics of the CVD process.

2.2 CVD coating growth rate

The deposition rate is mainly controlled by the mass transport of reactants through the stagnant layer by diffusion, and the surface reaction kinetics of the reactants. The CVD coating growth

rate v (ms^{-1}) can be analyzed by a reactants diffusion - surface reaction balancing model [30,31], according to:

$$v = \frac{k_S\, h_G}{k_S + h_G} \frac{C_G}{N} \tag{2.1}$$

where k_s is the surface reaction rate (ms^{-1}), h_G is the mass transfer coefficient (ms^{-1}), C_G is the concentration of the species in the gaseous phase in terms of number of atoms (m^{-3}), and N is the number of atoms of the species per unit volume in the solid film (m^{-3}).

If the surface reaction rate is much lower than the mass transport rate ($ks \ll h_G$), the CVD reaction is within the surface reaction control regime, and the deposition rate is mainly limited by the surface reaction rate k_s. Equation (2.1) becomes:

$$v_S = k_S \frac{C_G}{N} \tag{2.2}$$

If the surface reaction rate is much higher than the mass transport rate ($ks \gg h_G$), the CVD reaction is within the mass transport control regime, and the deposition rate is mainly limited by the mass transfer coefficient h_G. Equation (2.1) becomes:

$$v_G = h_G \frac{C_G}{N} \tag{2.3}$$

Equation (2.3) can be reformulated according to fluid dynamic theory [32], to be:

$$v_G \propto \frac{C_G}{N} D_G (u\rho)^{1/2} \tag{2.4}$$

where D_G (m^2s^{-1}) is the diffusivity of the gas molecules, u is the gas flow speed (ms^{-1}), and ρ is the gas density (kg m^{-3}). According to equation (2.4), the coating growth rate of the mass transport controlled deposition increases with higher precursor diffusivity, higher gas density and faster gas flow.

2.3 Low pressure chemical vapour deposition

Low pressure CVD (LPCVD) is a commonly used CVD technique that applies low pressures (tens to thousands of Pa) of the gaseous precursors, which is much lower compared to that (1

atm = 101325 Pa) of the atmospheric pressure CVD (APCVD). The lowered pressure in LPCVD is mainly to reduce the mass transport rate of reacting chemicals. According to equation (2.4), the rate of CVD deposition limited by the mass transport decreases with lower gas flow speed and lower density of gaseous precursors. A low-pressure gaseous environment in LPCVD thus provides lower gas densities and therefore suppresses the mass transport through stagnant layer diffusion. In addition, LPCVD decreases the dependence on the gas flow velocity, which helps to deposit films showing better uniformity and homogeneity. However, a disadvantage of LPCVD can be low coating growth rates. The CVD growth of TiAlN coatings is very flow dependent, where too high gas flow rate was found to cause microstructural inhomogeneities. Therefore, LPCVD with relatively low flow rates are used for depositing TiAlN coatings. The deposition of TiN coating is less flow dependent, and CVD processes with higher partial pressures of reactants can be used.

Paper I describes TiAlN coatings that were deposited by LPCVD in an industrial scale CVD equipment at 700 °C, and a pressure below 25 mbar (2500 Pa), where gaseous precursors $AlCl_3$, $TiCl_3$, NH_3 were supplied rotationally. Paper II deals with TiN coatings that were deposited in an industrial scale hot wall CVD reactor at 850 ºC, 900 ºC, and 950 ºC using $TiCl_4$ and H_2 precursors with a pressure of 400 mbar (40000 Pa).

3 Hard coating materials

To meet the demands of high temperatures and pressures during cutting operations, wear-resistant hard coatings are usually composed of several layers of different phases. Common hard CVD coating phases include TiC, TiN, TiCN, TiAlN, α-Al_2O_3, and κ-Al_2O_3. The mechanical performance can be tuned by designing the texture and microstructure of the coatings. The study in this thesis is focused on the CVD TiN and TiAlN hard coatings. One example of a cross section image of a CVD TiN-TiAlN-TiN multi-layered coating deposited on a cemented carbide (WC/Co) substrate is shown in Fig. 3.1.

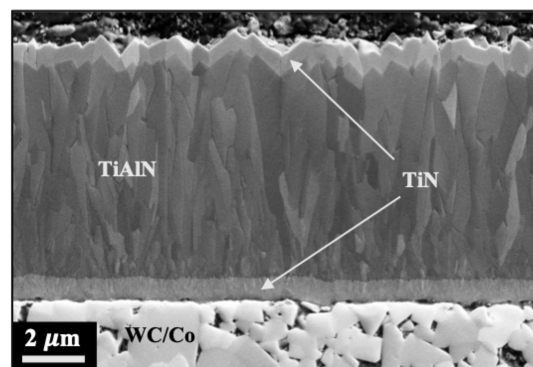

Figure 3.1. Cross section micrograph of a CVD TiN-TiAlN-TiN multi-layered coating deposited onto a cemented carbide substrate. The image was acquired using a scanning electron microscope.

3.1 Titanium nitride

TiN is a refractory material with face centered cubic (FCC) NaCl crystal structure, as shown in Fig. 3.2 (a). The lattice parameter of TiN is 4.24 Å. TiN has been widely used in various applications, such as diffusion barriers [33], corrosion protective layers [5], and wear-resistant coatings [34], due to its superior hardness, thermal stability, corrosion and wear resistance. TiN coatings can be synthesized by both Physical vapour deposition (PVD) [35,36] and CVD [37]. In papers I and II, TiN was deposited onto cemented carbide and multi-element alloy substrates, by CVD using $TiCl_4$, N_2 and H_2 as precursor and carrier gases, based on the following reaction [37]:

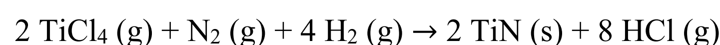

$$2\ TiCl_4\ (g) + N_2\ (g) + 4\ H_2\ (g) \rightarrow 2\ TiN\ (s) + 8\ HCl\ (g)$$

TiN exhibits good adhesion to a cemented carbide substrate. Therefore, TiN is commonly deposited as an intermediate layer prior to the deposition of TiCN and TiAlN coatings. In paper II, the capability of coating TiN using CVD onto a CoCrFeNi MPEA substrate is evaluated, and grain boundary diffusion of substrate elements into the TiN coating is analyzed. However, TiN coatings exhibit less prominent oxidation resistance, where oxidation starts from 550 ^{o}C, which is much lower than that of the cutting operation environment [12].

3.2 Titanium aluminium nitride

As shown in Fig. 3.2 (b), by partly replacing Ti atoms in the TiN crystal with Al atoms, the ternary alloy $Ti_{1-x}Al_xN$ (TiAlN) is formed (x represents the occupancy of Al atoms on the metal lattice), which can be seen as a solid solution phase of cubic TiN (c-TiN) and cubic AlN (c-AlN). It has been reported that by increasing the Al content, mechanical properties and chemical inertness of the TiAlN coatings, such as hardness, hot hardness, and oxidation resistance, increase prominently compared to that of the TiN phase [12,38]. Cubic Al-rich phases (AlN, and TiAlN) are metastable. PVD was originally used for depositing $Ti_{1-x}Al_xN$ coatings, yielding restricted Al contents up to $x \sim 0.67$ [39,40]. A higher Al content in PVD TiAlN coatings results in the formation of hexagonal wurtzite AlN (h-AlN) phase. However, in recent years c-TiAlN coatings with higher Al content ($x \geq 0.9$) have been synthesized by LPCVD [38], with higher hardness and better oxidation resistance. The thermal stability of TiAlN is essential for cutting tool applications, and the metastable cubic TiAlN phase was reported to undergo decomposition at elevated temperatures [41,42]. However, LPCVD TiAlN with high Al content was shown to exhibit better thermal stability than PVD TiAlN, and the cubic phase remains stable at temperatures up to ~ 1000 ^{o}C [38,43].

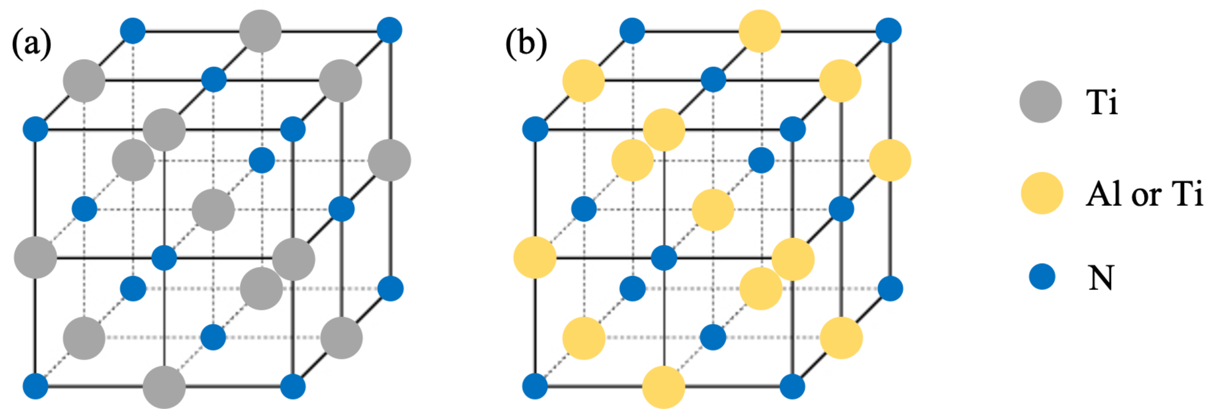

Figure 3.2. Schematics of the crystal structures of TiN and TiAlN. (a) cubic TiN where Ti and N atoms form two FCC sublattices; (b) TiAlN structure where Al atoms partly replace the Ti atoms in the Ti FCC sublattice in the TiN crystal structure. The Al content is represented by the occupancy x in $Ti_{1-x}Al_xN$. Vacancies of Ti, Al, or N are not presented.

In paper I, the TiAlN coating was synthesized by LPCVD on a cemented carbide substrate pre-coated with TiN. The gaseous precursors, $AlCl_3$–$TiCl_4$–NH_3, are supplied rotationally in an industrial equipment, which was found to yield a periodic structure along the [001] directions, consisting of nanolamellae with different Al and Ti contents. Both the Al-rich (Al(Ti)N) and the more Ti-rich (Ti(Al)N) lamellae have the cubic structure without significant lattice mismatch [7,43,44]. The atomic resolution scanning transmission electron micrograph collected by high angle annular dark field (HAADF) detector, as shown in Fig. 3.3, illustrates the typical nanolamella structure. The contrast mechanism will be described in Chapter 4. The formation of the nanolamellae were suggested by Paseuth, *et al.* to be due to a short-range diffusion of the spinodal decomposition during the fast deposition process [44]. Alternatively, a kinetically controlled self-assembly process during the surface reaction [45] was reported to cause the coherent nanolamella structure [7]. In addition, nanolamella structures with periodic cubic Ti(Al)N and h-AlN were also reported to exist in LPCVD TiAlN coatings [46,47]. Apparently, the growth mechanism of the LPCVD nanolamella TiAlN phase has not been fully revealed and much research remains to understand it.

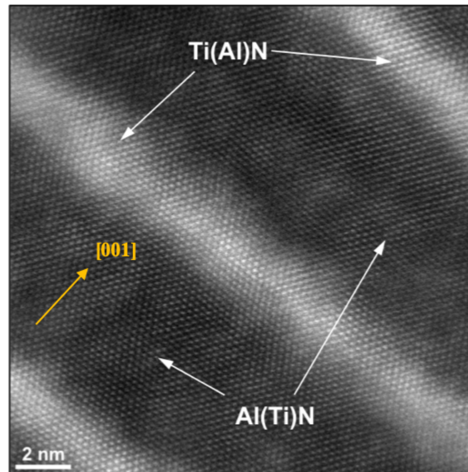

Figure 3.3. High resolution scanning transmission electron micrograph of the nanolamella TiAlN structure, collected by the HAADF detector. Thin layers with bright contrast are Ti(Al)N phase, thicker layers with dark contrast are Al(Ti)N phase.

3.3 Aluminium nitride

h-AlN is a typical III-V semiconductor material with a wurtzite structure and a wide direct band gap of 6 eV [48]. With such a large band gap, h-AlN has been intensively used in opto-electronic devices, such as light emitting diodes, laser diodes and photodetectors. The h-AlN is also used in high-temperature electronic devices because of its high melting temperature [49]. It is also widely used in electronic industries for semiconductor packages due to its high thermal conductivity at elevated temperature and a good thermal expansion match with silicon [50].

The h-AlN phase was found co-growing with the cubic TiAlN phase during the CVD synthesis process, which is believed to cause inferior mechanical performance of the hard coating. h-AlN shows high hardness (~ 15 GPa) [8,9], which is however still much lower than that of the cubic TiAlN (~ 30 GPa) [38]. Synthesizing cubic TiAlN coatings with high Al content thus has been a challenge, because of the possible co-formation of the h-AlN phase. Grain morphology distortions were reported to appear in PVD coatings, where a mixture of TiAlN and a noticeable amount of h-AlN was found to result in the disappearance of the TiAlN columnar grain morphology [39,51]. In paper I, a co-growth of h-AlN onto the Ti(Al)N lamellae is identified, and it is believed to cause the microstructural inhomogeneity of the TiAlN coating. The results will be discussed in Chapter 5.

4 Experimental procedure

The main part of this thesis is concerned with electron microscopy, which, as a powerful technique for materials characterization. It provides the possibility for combining high resolution imaging with crystallographic and chemical information. In this research, both scanning electron microscopy (SEM) and transmission electron microscopy (TEM) are used for the microstructure investigations. Basic theories of electron microscopy are discussed in this chapter. In addition, X-ray diffraction (XRD) is also used in this thesis to analyze phase contents and coating textures. A brief introduction to some modelling techniques is included as well.

4.1 X-ray diffraction

XRD was used to examine the phase contents and coating textures [52,53]. As schematically illustrated in Fig. 4.1, an X-ray source generates an incident beam to illuminate a polycrystalline or powder specimen, and the incident X-rays are diffracted by the crystal structure according to Bragg's law: $\lambda = 2d_{hkl} \sin\theta$, where d_{hkl} is the interplanar distance between (hkl) atomic planes, λ is the wavelength of the X-rays, and θ is the Bragg angle. The diffracted beam is detected by an X-ray detector, and the angle between the incident beam and the diffracted beam is 2θ. During a θ - 2θ scan, the sample and the detector rotate with an angular speed of ω and 2ω, respectively, and the intensity I at the detector position is registered. The intensity I as a function of 2θ is then presented as an X-ray diffractogram [52]. The XRD measurements for TiAlN coatings and TiN coatings were carried out by our project partners at Walter AG, Germany, and Uppsala University, Sweden, respectively.

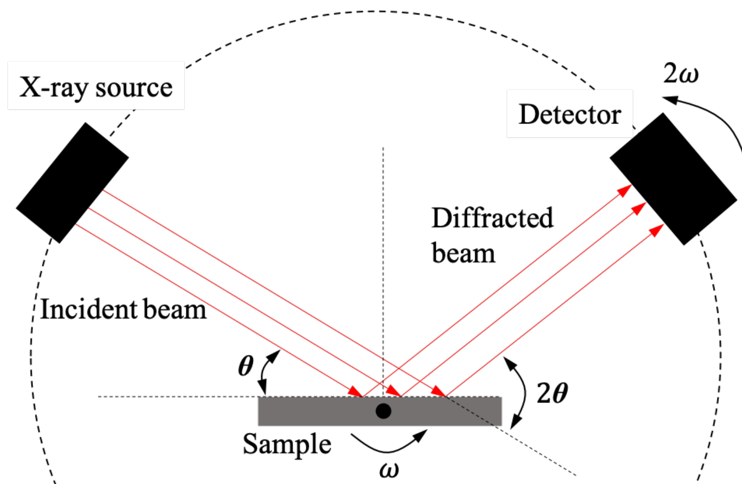

Figure 4.1. Schematic illustration of an X-ray spectrometer for a θ - 2θ scan.

4.2 Scanning electron microscopy

The basic configuration of an SEM is schematically illustrated in Fig. 4.2 (a). In an SEM, electrons are emitted from an electron source, usually a thermionic gun or a field emission gun (FEG). The stream of emitted electrons is accelerated by an anode below the gun, to an energy typically ranging from 2 to 30 keV. The electron beam is then converged by one or multiple electromagnetic condenser lenses and focused into a fine probe. The focused probe on the specimen surface is a demagnified image of the electron source. The convergence angle of the electron probe is determined by the objective aperture. By a beam shifting function using the scanning coils, the focused electron probe scans through a rectangular raster over the sample surface area of interest. The focused electron beam hits the sample surface and interacts with the specimen by elastic and inelastic scattering within a so-called interaction volume, as shown in Fig. 4.2 (b). Within the interaction volume, signals are generated, and may travel to the specimen surface, depending on where in the interaction volume the signal is generated. The signals emitted from the surface are detected by various detectors. Typical signals include Auger electrons (AEs), secondary electrons (SEs), back scattered electrons (BSEs) and characteristic X-rays. The detector signals will be processed by a computer that also controls the scanning circuit to control the position of the focused probe.

As shown in Fig. 4.2 (b), the interaction volume starts from the sample surface and expands down into the sample interior for a certain depth depending on an integral effect of specific material composition and the acceleration voltage. However, the escape depths of signals depend on their mean free paths within the specimen. SEs are generated by the inelastic scattering of the incident electrons, which excites the outer shell electrons of the specimen. SEs exhibit low energies (0 ~ 50 eV) and are easily reabsorbed within the specimen, which means that the SE signal detected by the detector is usually very localized, emitting from a volume that is a few nm deep from the specimen surface. An SE detector and an in-lens detector lying within the objective lens collect SEs, yielding micrographs of surface topographic information with high spatial resolution and sharp surface morphology contrast [54]. BSEs are incident electrons scattered by the nuclei of specimen atoms, with higher energies than the SEs. The BSEs are emitted from a larger part of the interaction volume, thus giving a worse spatial resolution compared to the SE signal. BSEs collected by an BSE detector provide image contrast depending on the local average atomic number since the probability of elastic scattering

increases with the atomic number, which means that an area with heavier elements generates more BSEs and yields a brighter contrast than an area with lighter elements.

Upon illumination by the primary electron beam, sufficient energy can be transferred to a core-shell electron that is excited outside the strong field of the nucleus, which is called ionization [55]. Once ionized, the excited atom can decay to the ground state where an outer shell electron fills the core hole, emitting excess energy. This transition energy can either create characteristic X-rays or AES. These AEs are emitted from a few top layers of atoms of the specimen surface, however, the signal intensity is too low to be detected by regular SEM detectors. Characteristic X-rays are emitted from a larger part of the interaction volume, and can be collected by a diode-type Si detector to perform XEDS. The SEM XEDS provides both qualitative and quantitative information about the chemical composition of the probed area, but with lower spatial resolution than the electron signals. The XEDS analysis is mainly performed in this thesis during scanning transmission electron microscopy (STEM) mode, and more details of STEM XEDS will be discussed in Section 4.3.4.

SEM was used in this thesis mainly for imaging the cross section to characterize the coating morphology, as e.g. the columnar coating grains shown in Fig. 3.1. The SEM results were acquired using Zeiss Supra 40VP, Ultra 55, and Crossbeam 540 systems, with in-lens and standard SE detectors.

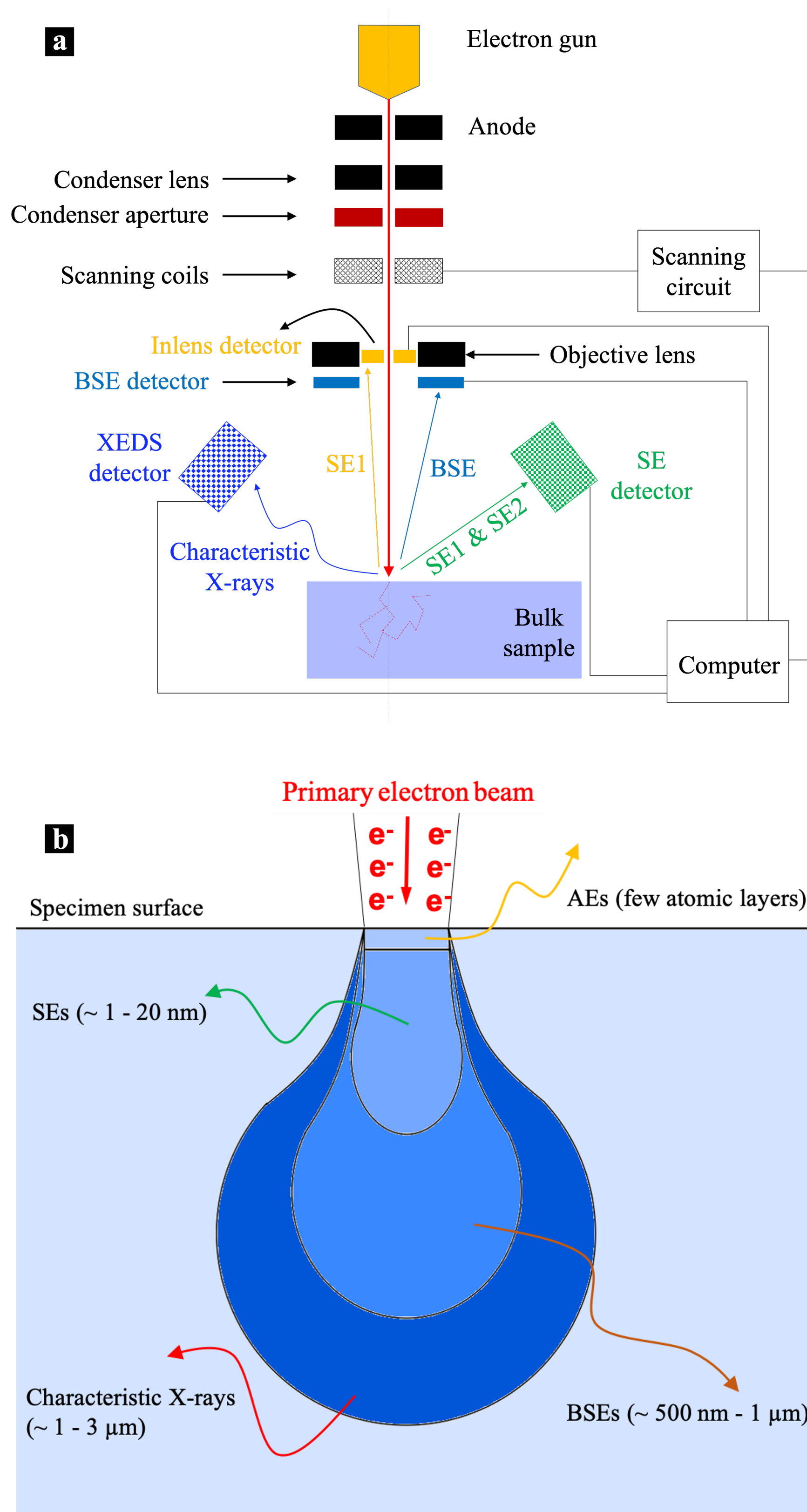

Figure 4.2. (a) Schematics of the SEM instrumentation. (b) Schematics of the electron beam - specimen interaction volume. Detected signals originate from a volume with a size that depends on the escape depth of the particular signal (not drawn to scale).

4.3 *Transmission electron microscopy*

The electron microscopy characterization in this thesis was mainly done by TEM, in both the transmission (TEM) and scanning transmission (STEM) modes. TEM is a powerful instrument that enables high spatial resolution imaging together with the acquisition of chemical and crystallographic information. In this section, the regular configuration of a TEM instrument, and the principles of the TEM/STEM operations used in this research are presented.

4.3.1 *Instrument configurations*

The configurations of TEM differ slightly depending on each instrument, therefore this section will be focused on the instrument used in this research. In this work, TEM/STEM characterization was performed using an FEI Titan 80-300 TEM/STEM instrument, and the basic configuration is schematically shown in Fig. 4.3. A TEM mainly consists of three systems: the illumination system, the image formation system, and the projection and image recording system.

In the illumination system, the primary electrons are emitted from an electron gun. In this research, a Schottky FEG is used. It exhibits higher brightness than the thermionic gun, which enables a smaller probe size and a higher spatial resolution, as the source size can be significantly demagnified without severe loss of primary beam current [56]. The emitted electrons are then accelerated by an anode, and the microscope is mainly operated at 300 kV in this research. The condenser system is located below the electron gun. A strong C1 lens first collects electrons from a large solid angle and forms a demagnified image of the source. The electron beam current is mainly controlled by the C1 aperture and by tuning the C1 lens strength. The second condenser lens (C2) projects the demagnified image of the source formed by C1 onto the specimen, where the illumination area is controlled by C2 and the beam convergence angle by the C2 aperture. In older TEMs, the illumination area and convergence angle cannot be tuned independently by only the C2 lens and the C2 aperture. In newer TEMs, this is realized by introducing another condenser lens (C3) and a corresponding aperture (C3 aperture).

The image forming system is the most critical part of a TEM, mainly consisting of the objective lens and objective aperture. The objective lens is the most critical component of a TEM as it determines the resolving power of the microscope. The thin foil sample is usually immersed into the strong magnetic field created between the upper and lower polepieces of the objective

lens. A solid-state Si XEDS detector made of a reverse-biased p-i-n diode (‘p-doped’ – ‘intrinsic’ – ‘n-doped’) is mounted close to the sample in order to obtain a large solid angle for collection of characteristic X-rays. The transmitted electrons are collected to form an image in the objective lens image plane and a diffraction pattern in the objective back focal plane. The objective aperture in the objective back focal plane can be used for bright field (BF) and dark field (DF) imaging. A selected area diffraction (SAD) aperture can be inserted in the image plane to choose a specific area for electron diffraction.

The image or diffraction pattern formed by the image forming system is then collected by the projection and image recording system. This system consists of several lenses, including a diffraction lens, an intermediate lens, and a projection lens. High angle annular dark field (HAADF) and annular dark field (ADF) detectors are placed in the diffraction plane to collect transmitted electrons with different scattering angles for STEM imaging. The final image or diffraction pattern can be viewed on a fluorescent screen or recorded on a charge coupled device (CCD) detector. A Gatan image filter (GIF) system is mounted below the CCD camera for EELS and energy filtered TEM (EFTEM) operations. It consists of an entrance aperture, a magnetic prism, pre- and post-prism multipoles (tuning multipoles, and projection multipoles), an energy selecting slit and another CCD camera.

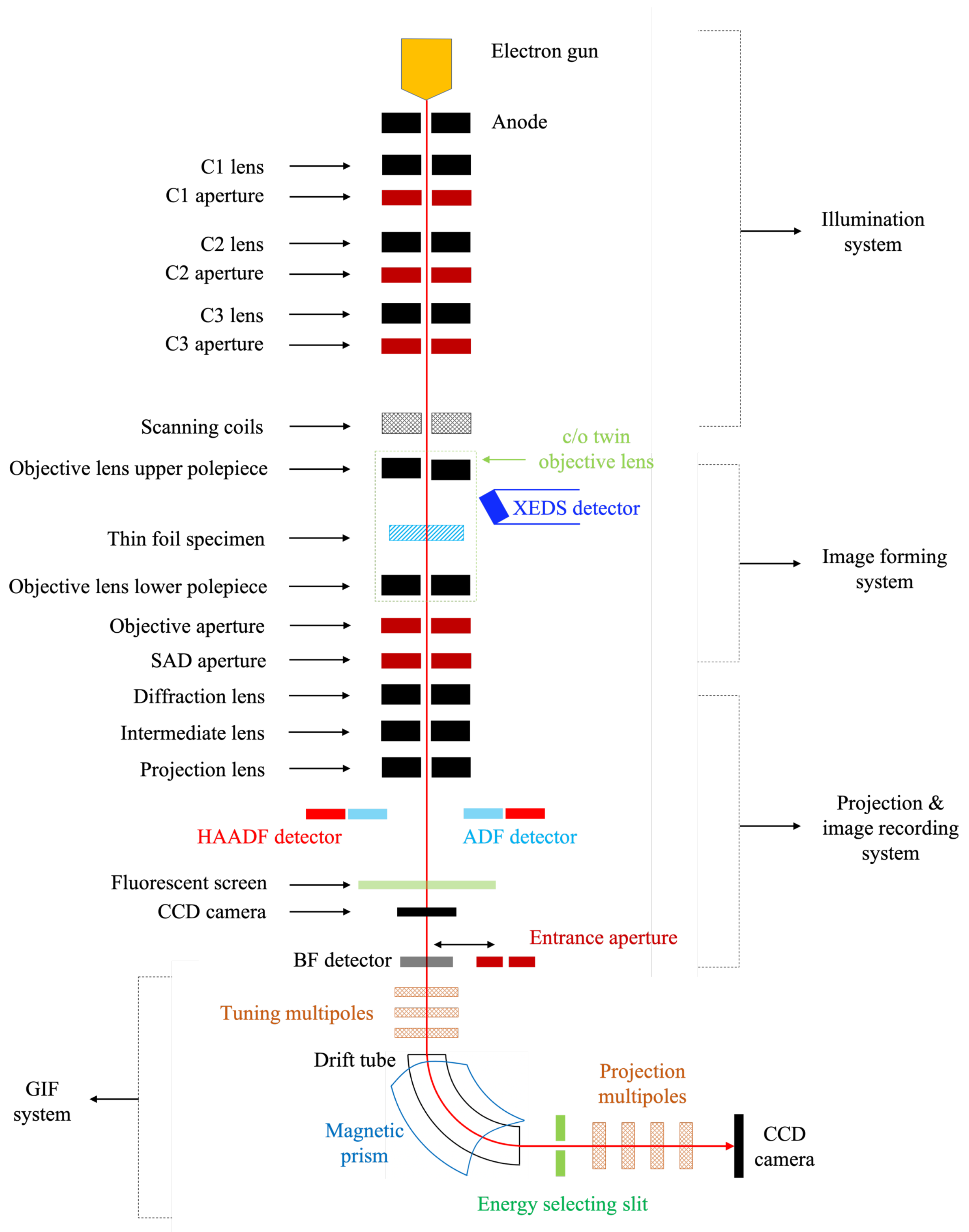

Figure 4.3. Schematics of basic TEM configurations. The TEM is mainly composed of the illumination system, image forming system, projection and image recording systems and the GIF system.

4.3.2 TEM mode

In TEM mode, a (nearly) parallel primary electron beam illuminates the thin foil specimen, which is typically around 100 nm thick. The high energy electrons scatter elastically and inelastically inside the specimen within a narrow interaction volume, as illustrated in Fig. 4.4. Backscattered signals, such as characteristic X-rays, SEs and BSEs, are emitted. Characteristic X-rays can be collected by the XEDS detector, closely mounted above the thin foil specimen. However, SE and BSE detectors are usually not implemented in TEM due to size restriction of the objective lens. TEM micrographs are formed by collecting electrons that are transmitted by the thin foil specimen.

Bright field (BF) imaging in the TEM is realized by inserting the objective aperture in the back focal plane of the objective lens, only allowing the direct beam to pass. The BF micrograph exhibits mainly mass-thickness contrast and diffraction contrast [55]. The mass-thickness contrast depends on the average atomic number $\bar{Z}$ and local specimen thickness t, where areas with greater $\bar{Z}$ and t scatter more electrons and therefore appear darker in the BF micrograph. For diffraction contrast, the BF micrographs appear darker at areas where the crystal orientation is closer to a Bragg condition with respect to the incident electron beam.

The elastically scattered electrons are deflected from the incident direction resulting in Bragg diffraction according to Bragg's law. Dark field (DF) imaging is realized by inserting the objective aperture in the back focal plane of the objective lens, and only allowing the electron beam of a certain diffracted angle range to pass. The DF micrographs mainly exhibit diffraction contrast, where areas closer to the Bragg conditions appear brighter [55]. Normal TEM imaging includes both the unscattered and the scattered electrons. High resolution TEM (HRTEM) is performed by using a large objective aperture (or no objective aperture), and it exhibits phase contrast with atomic spatial resolution due to interference of the direct beam and diffracted beams [56]. HRTEM is used in this work to reveal the crystal orientation, atomic arrangement and phase content in regions of interest.

The inelastically scattered electrons have lost energy through various inelastic scattering events, such as bulk plasmon excitation, inter- and intra-band excitation, core shell ionization, *etc* [55]. The inelastically scattered electrons can be recorded by a GIF system and employed for EELS and EFTEM measurements, which provide information regarding the chemistry and electronic structure of the specimen [55,57].

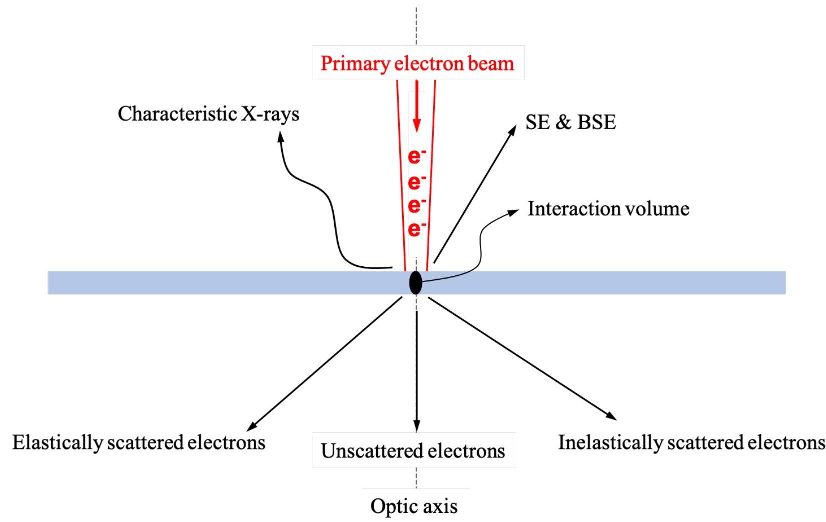

Figure. 4.4. Schematics of TEM signals originating from the interaction between the high energy electron beam and the thin foil sample.

4.3.3 STEM mode

In STEM mode, information is recorded by serial acquisition, where a rectangular area of the thin foil specimen is scanned by a convergent electron beam that is focused into a fine probe by the condenser lenses. Due to the much smaller illumination area compared to the TEM mode, the interaction volume in STEM mode is much smaller, which therefore enables high spatial resolution for various signals, as shown in Fig. 4.5. Characteristic X-rays from the narrow interaction volume can be recorded and form an XEDS spectrum image, which is a data set where each pixel of the image contains an XEDS spectrum. SEs and BSEs are usually not used in TEM for imaging, although high resolution SE imaging was reported being implemented by using an SE detector in an aberration-corrected STEM instrument [58]. However, normally STEM imaging is realized through collecting transmitted electrons with different scattering angles by detectors mounted in a conjugate back focal plane of the objective lens, below the projection lens. As shown in Fig. 4.5, the STEM BF mode is performed by collecting transmitted electrons that are unscattered (or scattered less than 10 mrad) from the optical axis using a BF detector. Similar to the TEM BF imaging, STEM BF imaging shows mass-thickness contrast and diffraction contrast. Annular dark field (ADF) imaging is performed using a concentric detector to collect transmitted electrons that are scattered from the optical axis between approximate 10 to 50 mrad, which contribute to the mass-thickness contrast and diffraction contrast. To exclude the Bragg diffracted electrons and only collect incoherent elastically scattered electrons, a larger concentric high angle ADF (HAADF) detector is used.

STEM HAADF imaging collects transmitted electrons with scattering angle higher than 50 mrad, which is similar to unscreened Rutherford scattering, where the scattering cross section increases with Z^2. However, due to the screening effect by the electron cloud, the Z dependence varies between $Z^{1.7}$ and $Z^{1.9}$ depending on the inner collection angle [59]. STEM HAADF imaging is widely used in this research to differentiate Ti-rich and Al-rich areas with high spatial resolution. As shown in Fig. 3.3, the Ti(Al)N lamellae with higher average atomic number appear brighter, and the Al(Ti)N lamellae with lower average atomic number appear darker.

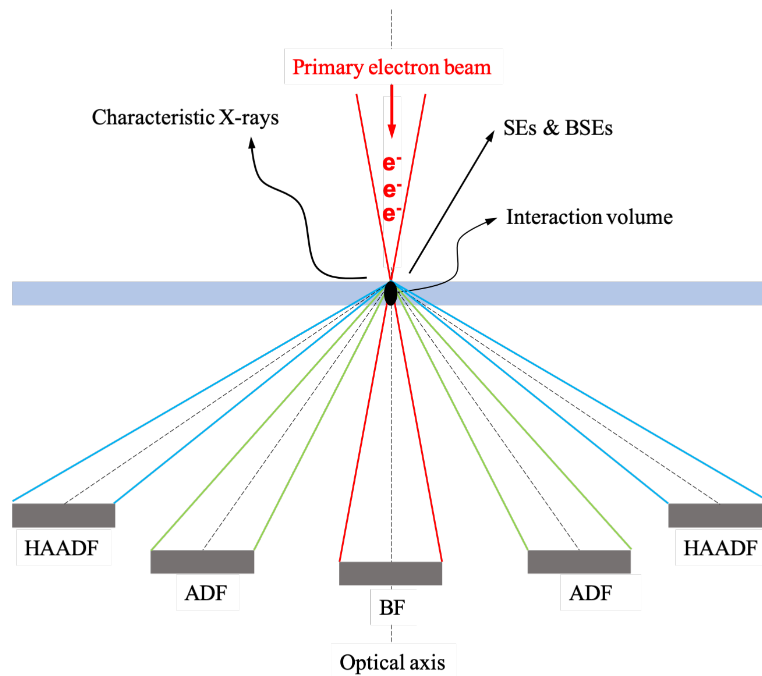

Figure. 4.5. Schematics of the STEM signals and detectors for various operating modes.

4.3.4 X-ray energy dispersive spectrometry

Analytical STEM XEDS is intensively employed in this study, which gives high spatial resolution for chemical analysis for a given region of interest. Atoms can be ionized by the high energy primary electron beam, where an inner shell electron is excited to the vacuum state leaving an inner shell hole. The relaxation to the ground state through transferring an outer shell electron to the inner shell hole can lead to the emission of characteristic X-rays with an energy unique to the atom. The innermost electron shell is called the K shell, the next is the L shell, and the next M, and so on. During the penetration of primary electrons through the specimen,

their momenta change substantially due to Coulomb interaction with nuclei, which emits the so-called Bremsstrahlung X-rays. The incident electrons can lose any amount of energy to produce Bremsstrahlung X-rays from zero to the primary beam energy, which therefore yields a continuous background in the XEDS spectra. X-rays emitted from the specimen are recorded by semiconductor detectors. The X-ray photons entering the detector can excite the semiconductor electrons from the valence band to the conduction band and cause electron-hole pairs. The energy for this process in Si is on average around 3.8 eV at liquid N_2 temperature. The X-ray energy is thus quantified by the number of electron-hole pairs. The energy resolution achieved by such type of detector is around 135 eV [55].

Both identification and quantification of chemical elements can be done from XEDS spectra. The elements in the specimen are typically identified by the location of their characteristic X-ray peaks in the spectrum, although the poor energy resolution (peak overlap) is sometimes a limit. For quantification of different elements, the Bremsstrahlung background of the XEDS spectrum needs to be subtracted. This background subtraction may, for example, be done through defining several background windows where no characteristic X-ray peaks exist, where the background is fitted by polynomial functions and extended to the remaining regions. Once the background is subtracted, the intensities of certain X-ray peaks for each element are integrated. Assuming I_A and I_B are the integrated peak intensities of elements A and B present in the specimen, the *Cliff - Lorimer* equation allows quantification of the ratio of these two elements as:

$$\frac{C_A}{C_B} = k_{AB}\frac{I_A}{I_B} \tag{4.1}$$

where the C_A and C_B are the concentrations of elements A and B in the specimen, the k_{AB} is the Cliff-Lorimer factor calibrated by standard samples [55]. In this research, XEDS quantification is widely employed to determine the ratio of various elements. The data processing is implemented by XEDS software packages. An example of the STEM XEDS analysis is shown below. An XEDS linescan is acquired across the TiN/TiAlN interface, as illustrated in Fig. 4.6 (a). Using the XEDS data, the spatial variations of Al and Cl are calculated, see Fig. 4.6 (b). The peaks of Al and Cl at the TiN/TiAlN interface indicate a co-enrichment of the Al and Cl, which in this case probably indicates an incomplete reaction of aluminium chlorides precursors that have diffused through the stagnant layer to the substrate surface during the CVD process.

The incomplete reaction causes an accumulation of Cl in the coating that should otherwise have been released to the gas phase. This is discussed further in Paper I.

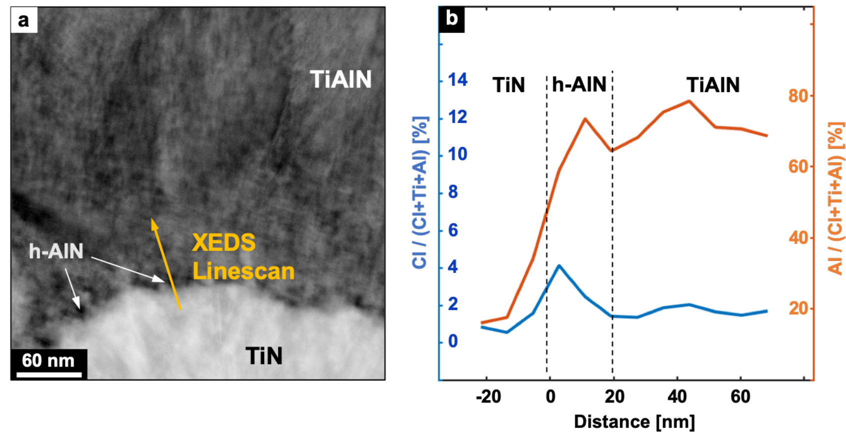

Figure. 4.6. Example of STEM XEDS analysis of the TiN/TiAlN interface. (a) STEM HAADF imaging of the TiN/TiAlN interface. An XEDS linescan is collected as illustrated by the arrow. (b) Variations of the Cl and Al ratios along the linescan shown in (a), obtained from the XEDS data.

4.3.5 Electron energy loss spectroscopy

STEM EELS is used in this study for element identification requiring both high spatial and high energy resolution that XEDS cannot achieve. Electrons may undergo various inelastic scattering events within the specimen. The energy of the transmitted electrons is recorded, and electron counts as a function of energy loss is displayed by the GIF system as an EELS spectrum. A typical EELS spectrum contains a narrow zero loss peak (ZLP), a low loss regime, and a core loss regime. The ZLP contains electrons that lose no (or very little) energy when penetrating the specimen, and the width of the peak defines the energy resolution of the recorded EELS spectrum [55,57]. The low loss region extends from the ZLP to 50 ~ 100 eV, which mainly contains plasmon peaks. The low loss spectra can be used to determine the sample thickness and to exclude the contribution of plural inelastic scattering to the ionization edge intensity for absolute element quantification [55,57]. After the low loss area is the core loss region, where the inner shell ionizations are shown as edges of the corresponding elements. The energy resolution of < 1 eV of EELS makes it possible to differentiate the Ti L_{23} edge (456 eV) from the N K edge (401 eV), which is used in paper I to identify the presence of elements to identify the various phases.

4.3.6 *STEM probe size and imaging resolution*

The spatial resolution of STEM imaging is mainly limited by the size of the convergent electron probe scanned across the specimen. According to Rayleigh's theory, the electron probe converged by an aperture is designated as an Airy pattern, assuming the primary beam is solely diffraction limited [56]. The probe radius limited by the illumination aperture effect, is given as:

$$r_d \approx 0.61 \frac{\lambda}{\alpha} \tag{4.2}$$

where r_d is the radius of the focused electron probe limited by diffraction, λ is the wavelength of the incident electron beam, and α is the convergence angle (in radians) of the incident beam. According to equation (4.2), the focused probe size decreases with shorter wavelength of incident electrons and with larger convergence angle. However, the imperfections of electromagnetic lenses also limit the size of the electron probe where the spherical aberration is the main factor and given by:

$$r_s \approx \frac{1}{4} C_s \alpha^3 \tag{4.3}$$

where r_s is the radius of the focused electron probe limited by spherical aberration and C_s is the coefficient of the spherical aberration. According to equation (4.3), the electron probe size increases with a larger convergence angle. The STEM probe size is also influenced by the chromatic aberration and effective source size, which however are negligible compared to the diffraction limit and the spherical aberration. As decreasing the size of illumination aperture suppresses the spherical aberration but leads to more diffraction effects, there is an optimal illumination aperture size that gives the optimal convergence angle α_{opt} for the smallest probe size and highest spatial resolution:

$$\alpha_{opt} \approx \left(\frac{4\lambda}{C_s}\right)^{1/4} \tag{4.4}$$

The spherical aberration cannot be corrected for by electromagnetic lenses, since no concave magnetic lenses exist. It thus has to be corrected by C_s correctors that contain a complex arrangement of multiple hexapoles, or octupoles, and quadrupoles [56]. Using the C_s corrector suppresses the spherical aberration, which allows a larger illumination aperture (C_2 aperture) and thereby suppresses the diffraction effect. The microscope used in this research is equipped

with a spherical aberration corrector for the condenser lens, which gives an ideal spatial resolution of around 1 Å that enables atomic scale HRSTEM imaging, which is used in this research to reveal the atomic arrangement, phase identity and crystal orientation in the sample.

4.3.7 Beam broadening and spectrometry/spectroscopy resolution

The spatial resolution of XEDS and EELS depends on the size of the interaction volume within the thin foil specimen, as shown in Fig. 4.7. In STEM mode, the convergent beam is a focused probe with a diameter of d. The beam propagating through the specimen broadens and exits the bottom surface with diameter of $R_{\max}$. The spatial resolution R for spectroscopy analysis is defined as the smallest distance between two interaction volumes that give independent spectra [55]:

$$R = \frac{(d + R_{max})}{2} = (d^2 + b^2)^{1/2} \tag{4.5}$$

where b is the electron beam broadening within the specimen and can be calculated as [55]:

$$b = 8 \times 10^{-12} \frac{Z}{E_0} (N_v)^{1/2}\, t^{2/3} \tag{4.6}$$

where t is the thickness of specimen, E_0 is the energy of primary electron beam, N_v is the number of atoms per unit volume, and Z is the atomic number (all variables in SI units except E_0 in keV). In STEM XEDS/EELS experiments, the spatial resolution is mainly limited by the beam broadening, which is typically 5 ~ 10 nm, instead of the nominal probe size. Therefore, higher current with larger probe size (few nm instead of Å) can be used to obtain more incident electrons to get a higher signal to noise ratio. For STEM XEDS analysis, a thicker sample provides higher X-ray counts for better statistics, which is essential for quantification. However, the beam broadening effect increases with specimen thickness and therefore lowers the spatial resolution of the analysis.

The spatial resolution of chemical analysis can be measured experimentally by scanning the probe across an interface with an atomically discrete composition change, as shown in Fig. 4.7. The elemental profile determined experimentally is a convolution of the actual atomically sharp interface with the beam shape. Defining L by measuring the distance on the profile between the 2% and 98% points, the spatial resolution is [55]:

$$R = 1.414\,L \tag{4.7}$$

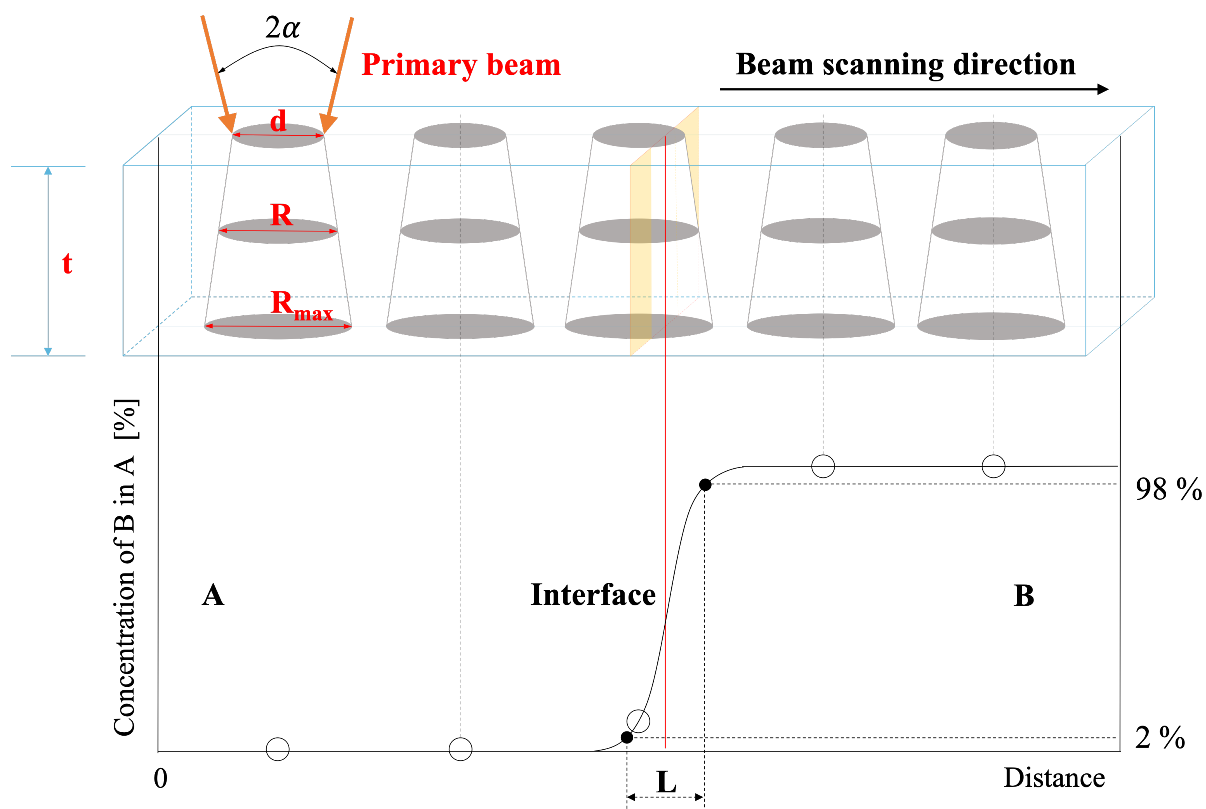

Figure 4.7. Schematic diagram illustrating the influence of the beam broadening effect on the spatial resolution of the STEM XEDS and EELS analysis.

The intensity of XEDS and EELS signals should also be considered for the actual spectroscopic studies. As illustrated in Fig. 4.8, the characteristic X-ray photons are emitted uniformly in all space. A collection solid angle $\pi\rho^2$ for X-ray photons usually only allows capturing of 0.01% ~ 1% of the emitted characteristic X-ray photons, although the XEDS detector is mounted as close to the specimen as possible and the take-off angle φ is optimized to maximize the collection efficiency. Therefore, higher beam currents and/or thicker samples can be used in XEDS acquisition for better counts, which however deteriorates the actual spectroscopic spatial resolution due to larger probe size and more beam broadening.

The inelastically scattered electrons are significantly forward scattered, and a small collection solid angle $\pi\beta^2$ (limited by the entrance aperture of the electron energy loss spectrometer) for the EELS signal makes possible a 50% ~100% collection efficiency. A small beam current and a thin specimen can yield sufficient counts for EELS acquisition with high spatial resolution.

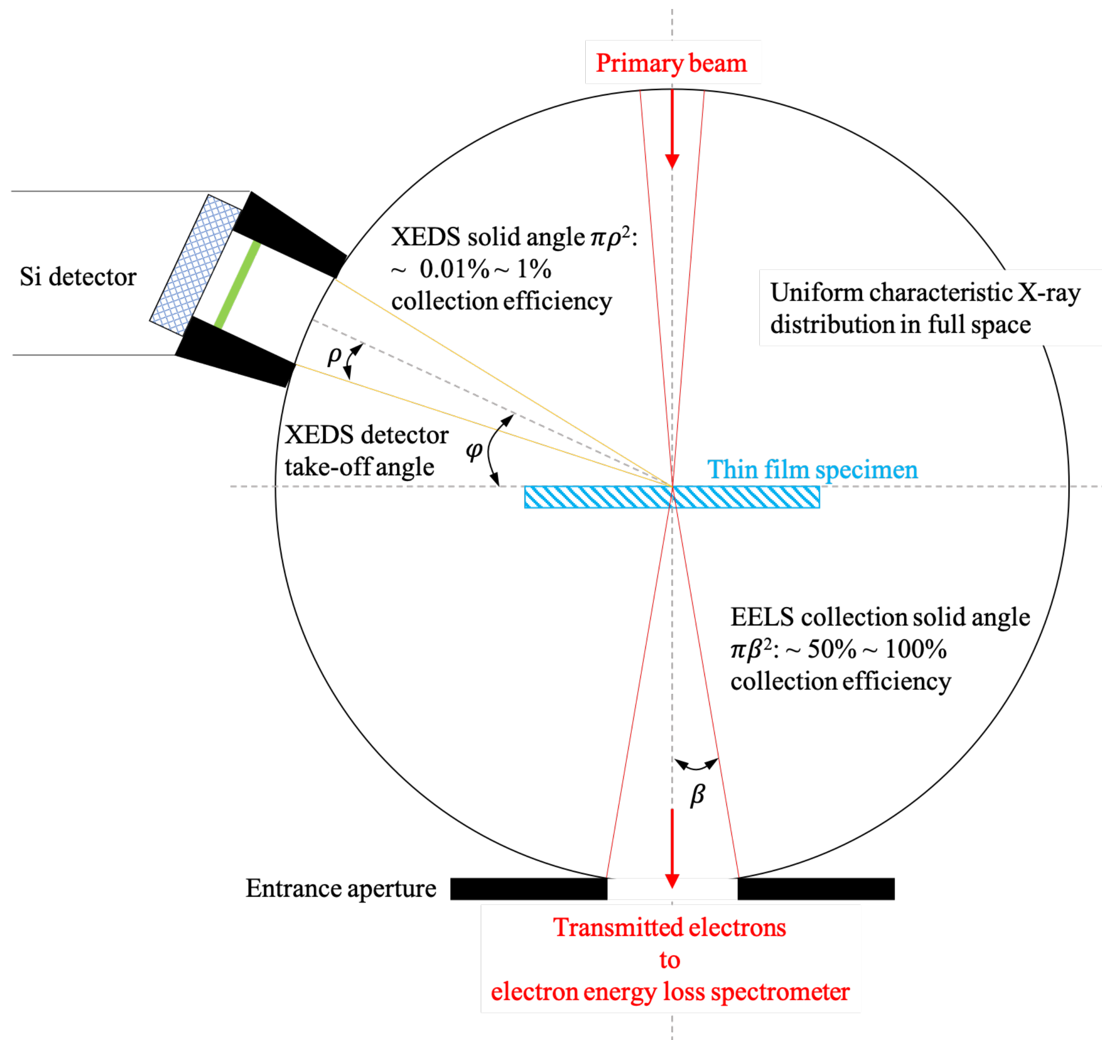

Figure 4.8. Schematic illustration of collection efficiencies of STEM XEDS and EELS. The characteristic X-ray photons are almost uniformly emitted in space. The energy loss electrons are strongly forward scattered and can be collected with high efficiency by a small collection angle.

4.4 Focused ion beam technique

The focused ion beam – scanning electron microscope (FIB-SEM) consists of an electron column for SEM functions, and an ion column mounted at an angle (usually 52°) with respect to the electron column [60]. As shown in Fig. 4.9, the sample is placed on the coincidence point were the electron and ion probes meet. The working distance between the coincidence point and the polepiece of the electron gun is usually around 10 mm. The ion column contains a Ga liquid ion metal source that emits Ga^+ ions, which are focused into a probe onto the specimen surface by an optical system of a similar design as in a SEM. The electron beam is used for imaging the specimen as in regular SEMs. The Ga^+ ion beam can be used for milling away

material by interaction between Ga^+ ions with the material, and SEs can be generated during the interaction and used for imaging. Deposition of a Pt-containing protective layer can be performed by introducing a Pt containing organometallic compound in gas form into the chamber in the vicinity of the sample surface. This gas interacts either with the electron or Ga^+ ion beam that scans over the area of interest, and a Pt containing layer, typically $20\ \mu m \times 2\ \mu m \times 2\ \mu m$, is deposited onto the sample surface. The Pt deposition is widely used for protecting site specific TEM lift-out samples, and to weld the sample to a micromanipulator or a TEM specimen grid. The recipe details for preparing the TEM lift-out thin foil specimens is described in references [61,62]. An FEI Versa 3D FIB-SEM equipped with a micromanipulator is used in this project mainly to prepare the site-specific TEM lift-out samples, and to mill coating cross sections for electron backscattered diffraction (EBSD) measurements.

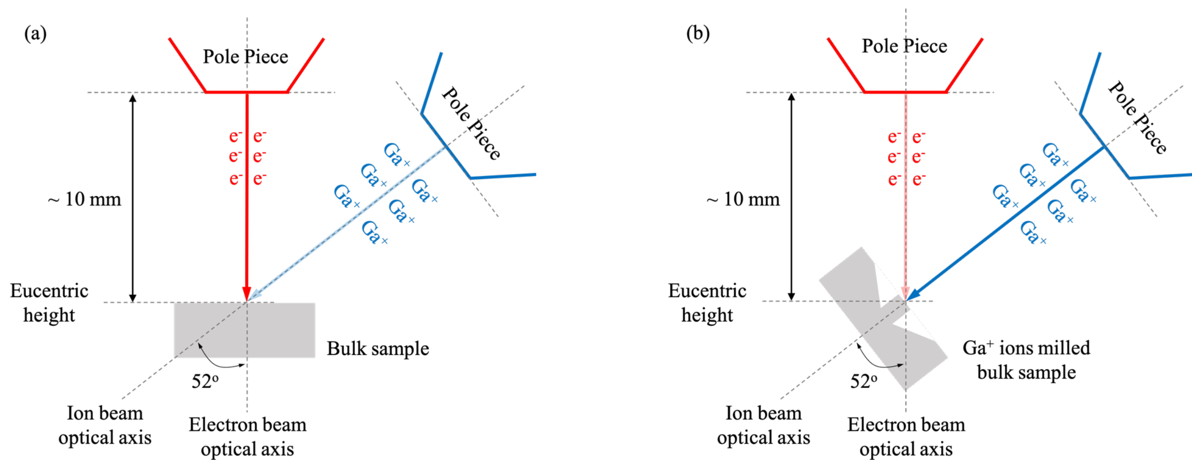

Figure 4.9. Schematics showing the basic principles of a FIB-SEM system. (a) Imaging by the electron beam. (b) Milling by the Ga^+ ion beam.

4.5 Electron backscattered diffraction and transmission Kikuchi diffraction

EBSD is a technique implemented in the SEM, where the BSEs are Bragg scattered and form Kikuchi bands onto an EBSD detector. The collected Kikuchi band patterns are then processed, including frame averaging and background subtraction. The processed Kikuchi band patterns are then indexed, through which local phases and orientations of areas of interest can be identified [63]. As shown in Fig. 4.10, in EBSD experiments, the bulk sample surface is tilted by around 70° to face the detector. The spatial resolution of EBSD depends on the size of the interaction volume that Bragg diffracted BSEs escape from, where a spatial resolution of 20 ~

50 nm can be achieved. The working distance between the scanned area on the sample surface and the polepiece in EBSD measurements is usually around 15 mm.

Transmission Kikuchi diffraction (TKD) technique is another SEM-based technique, where a thin foil sample is mounted with a 20° tilt, and the transmitted electrons that are first scattered sideways and then Bragg diffracted are collected by the EBSD detector. The working distance between the scanned area on the sample surface and the polepiece in TKD measurements is usually around 5 mm. Due to the small interaction volume in the transmission mode, the spatial resolution of TKD is higher than that of EBSD, and diffraction data from domains less than 10 nm can be achieved [64]. Due to larger interaction volumes for bulk samples, the BSEs undergo more inelastic scattering events and therefore exhibit broader energy spread in EBSD experiments. The broader distribution of energies and wavelengths of BSEs makes the Kikuchi patterns blurry and deteriorates signal to background ratio. However, in TKD the transmitted electrons undergo fewer inelastic scattering events within the small interaction volumes, and the recorded signal has less energy spread and a higher signal to background ratio. Therefore, TKD can provide Kikuchi patterns of higher quality than EBSD [64].

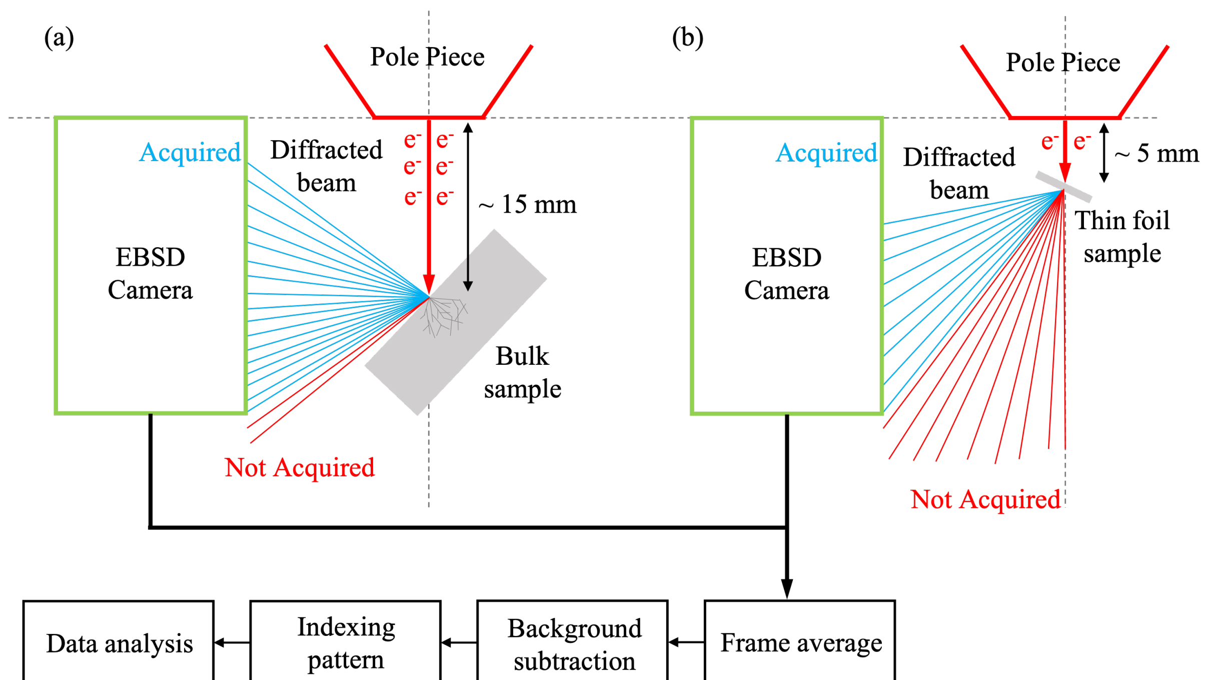

Figure 4.10. Schematics showing the basic geometries of the (a) EBSD and (b) TKD experimental setups.

4.6 Modelling considerations

4.6.1 Computational fluid dynamics

Computational fluids dynamics (CFD) simulations solve problems regarding the flow of fluids (liquids and gases), where various physical properties of the fluids including pressure, temperature, velocity, *etc*, are considered for simulating the heat and mass transport. A 3D model of the system is built and meshed, where each mesh consists of fluid cells for fluid flow analysis and solid cells for heat conduction analysis. The mass transport is calculated by numerically solving the Navier-Stokes equations for the fluid cells, and the heat transfer is calculated for the solid cells by solving the heat equation derived from the Fourier's law [65].

In paper I, the microstructural inhomogeneities in the TiAlN coating are found to be influenced by the precursor gas flow rate. Therefore, to correlate the microstructures of different locations on the cutting tool insert to the corresponding local gas flow rate, a CFD simulation was performed by Walter AG, Germany, using a Solidworks Flow Simulation software, to determine the gas flow patterns during the LPCVD process for the deposition of TiAlN coatings in a hot wall CVD reactor.

4.6.2 Density functional theory

Density functional theory (DFT) is a first principle method to understand the physical properties of condensed matter, where the electronic structures are calculated based on Schrödinger's equation. In theory, it is possible to derive all properties of a system by determining the many-body wave function, which is a function of all the coordinates of electrons and nuclei in the system. This turns out to be impossible in reality due to the limited computing power, and thus approximations must be made to simplify the problem. The first common approximation is the Born-Oppenheimer approximation, which treats all nuclei as fixed [66]. However, solving directly the Schrödinger's equation of a system with n electrons requires to determine a many-body wave function with $3n$ variables that involve the three coordinates of each electron, and it becomes intractable for more than a handful of electrons. To solve this problem, the Hohenberg-Kohn theorems were proposed, stating: (a) all properties of the system are uniquely determined by the ground state electron density; (b) an energy functional of the electron density exists, and the ground state electron density can be determined according to the minimum of the energy functional [67]. The Hohenberg-Kohn theorems therefore simplify the problem of solving the many-body wave function with 3n variables into a problem of determine the ground state

electron density with 3 variables, which is tractable for a system with hundreds of electrons. More technique details of the DFT simulations can be found in reference [67].

In this work, DFT simulations were performed by colleagues from the Royal Institute of Technology, Sweden, using the Vienna *ab-initio* simulation package (VASP) [68]. In paper I, a co-growth of h-AlN onto the Ti(Al)N lamellae with a specific crystallographic orientation relationship was found by electron microscopy. DFT modelling was performed to calculate the interface energies of the h-AlN/Ti(Al)N and the h-AlN/Al(Ti)N interfaces, which helped to explain the formation of the h-AlN in the TiAlN coatings. In addition, the adsorption energies of the reacting gas species (aluminium chlorides and titanium chlorides) onto the cubic TiN, $Ti_{0.5}Al_{0.5}N$, $Ti_{0.1}Al_{0.9}N$, and AlN phases were calculated, to help to understand the surface kinetics of the Al and Ti deposition.

4.6.3 Thermodynamic modelling

In thermodynamic modelling, a phase is usually considered as a mixed solution of several solutes of the constitute elements. The Gibbs energy of a phase is usually expressed as a collection of polynomials consisting of the initial Gibbs energies of pure solutes, the Gibbs energies caused by mixing, and extra terms that describe the interactions of elements in a certain phase. The Gibbs free energy of each phase is a function of temperature, pressure, and composition. The phase diagram calculation is to predict the existence and the compositions of the corresponding phases in a system, by minimizing the total Gibbs energy of the system at each given temperature and pressure. For thermodynamic modelling, it is essential to know the Gibbs energy polynomials of the studied phases, which are implemented in thermodynamic databases [69].

In paper II, phase diagrams were calculated by colleagues from the Royal Institute of Technology, Sweden, using the Thermo-Calc software [70]. The thermodynamic calculations predict the existence of stable phases that contain the components of the CoCrFeNi substrate, and the fraction of metal chlorides formed during the CVD process at different temperatures. The STEM XEDS measurements together with the thermodynamic simulation indicate that Cr would deplete from the substrate and diffuse into the coating.

5 Results and discussion

In this thesis, two coating systems were studied. In paper I, the detailed microstructure of LPCVD TiAlN coatings were investigated by various electron microscopy techniques with complementary DFT and CFD simulations, and a gas flow effect on the coating structure inhomogeneity is discussed. In paper II, the microstructure of TiN coatings deposited on a CoCrFeNi MPEA substrate was characterized, where a diffusion of Cr from the substrate to the coating through grain boundaries was revealed. Important results of the two papers will be discussed briefly in the following sections, while more details are given in the appended papers.

5.1 Co-growth of h-AlN and TiAlN phases

The h-AlN phase was found to grow together with the c-TiAlN phase, either as a thin layer at grain boundaries or as domains within the TiAlN grains. The h-AlN domains start growing on the (001) surface of the Ti(Al)N lamella, following an orientation relationship: $[110]_{cub}$ // $[2\bar{1}\bar{1}0]_{hex}$, and $(001)_{cub}$ // $(0001)_{hex}$. The formation of h-AlN on the Ti-rich TiAlN can be explained by the DFT modelling, where the h-AlN has a noticeably lower interface energy with the Ti(Al)N phase than with the Al(Ti)N phase. The h-AlN was also found to influence the growth of cubic nanolamellae. It is believed to be related to a grain morphology distortion in the TiAlN coatings, where a co-growth of h-AlN and the cubic TiAlN was found to result in a coating structure without columnar grain compared to the columnar grain morphology of the pure c-TiAlN phase.

5.2 Gas flow effect on Ti and Al deposition

According to the chemical analysis by STEM XEDS and CFD simulations of the gas flow, higher Ti/Al ratio than the average content ($Ti_{0.2}Al_{0.8}N$) appears at positions with faster gas flow, especially at the insert edge corner. The spatial variation of the Ti/Al ratio can be explained by the fact that the deposition rates of Ti and Al are influenced by the mass transport and the surface kinetics. As has been reported, the CVD reaction temperature for titanium chlorides is around 800 ^{o}C. This is much lower than that for the aluminium chlorides, which are deposited at around 1000 ^{o}C [37,71]. The temperature used in our LPCVD process is relatively low (~ 700 ^{o}C). It is sufficiently high for the surface reactions of the Ti deposition, and gives a mass transport controlled deposition. However, this low temperature limits the surface reactions of the Al deposition, which is thus confined to the surface reaction controlled

regime.

According to CVD fluid dynamic theories, a thinner stagnant boundary layer is formed due to the fast gas flow rate close to the insert corner [72]. Therefore, the mass transport of both the titanium and aluminium chlorides is stimulated by shortening the diffusion path through a thinner stagnant layer. According to equation (2.4), the rate of Ti deposition, which is mass transport controlled, increases with the square root of the gas flow velocity. However, for the deposition of Al that is limited by the surface reaction kinetics, the deposition rate is not increased by the higher local supply of the precursors. These facts explain the higher Ti/Al ratio at positions where the gas flow is faster.

5.3 Microstructural inhomogeneity in TiAlN coatings

An inhomogeneity of the TiAlN coating was reported in paper I, where columnar grains form at positions away from the edge corner, where the gas flow rate is lower. However, microstructural distortion appears at areas close to the insert corner, with higher Ti content than the average composition. PVD TiAlN coatings have also been reported to show grain morphology distortions, where a pronounced amount of the h-AlN was found to co-grow with the c-TiAlN phase and the columnar grains disappeared [39,51]. A similar effect in CVD TiAlN coatings was also found in our research, where a mixture of discontinuous cubic nanolamellae and h-AlN domains is suggested to cause the distortion of the columnar grains. According to our DFT simulations, h-AlN phase prefers to grow on Ti(Al)N, following the orientation relationship described above. It is thus suggested that the excessive h-AlN growth is caused by the high local Ti content. To summarize, the high gas flow speed stimulates the Ti-deposition and forms more Ti(Al)N phase. The excessive Ti(Al)N phase probably stimulates the formation of the co-grown h-AlN, which influences the formation of the nanolamellae structure and the columnar grain morphology.

5.4 Diffusion of Cr from a FeCrCoNi substrate through TiN grain boundaries

The microstructure of TiN grains grown by CVD on a FeCrCoNi multi-principal element alloy substrate was studied in paper II. Diffusion of Cr from the substrate was revealed by analytical electron microscopy. STEM XEDS showed the presence of Cr aggregated along the boundaries of the TiN grains. In addition, Cr was shown to be present at the coating top surface as well. This Cr enrichment may be due to the N-rich atmosphere present during the cooling process,

where the N-rich environment is suggested to cause a continuous diffusion of Cr towards the coating surface.

6 Future work

This thesis is focused on understanding the microstructure of CVD TiN coatings and LPCVD nanolamella TiAlN coatings. The detailed electron microscopy studies will in the future be broadened into other CVD coating systems, like TiCN and α-Al_2O_3 coatings. A few projects that have been planned are described in this chapter.

6.1 Quantification of chemical compositions of TiAlN nanolamellae

To fully understand the formation mechanism of the periodic TiAlN nanolamellae from CVD, it is necessary to determine the chemical composition of the nanolamellae. High spatial resolution for the chemical analysis is necessary to study the nanolamella structure, which can be implemented by analytical microscopy in STEM mode. The Ti and Al contents of the Ti(Al)N and Al(Ti)N lamellae have been determined using STEM XEDS, as shown in paper I. However, considering the nonstoichiometric composition of $Ti_{1-x}Al_xN_{1-y}$, the N content is still unknown. Due to the overlapping of N K_α (392 eV) peak with Ti L_α (452 eV) peak and limited energy resolution of XEDS (~ 130 eV), it is very difficult to quantify N by XEDS. EELS is thus planned to be used to determine measure the Ti and Al contents. A TiN sample with known composition was used to calibrate the cross-section ratio of the Ti L_{23} and N K edges. For accurate spectrum background subtraction and edge counts calculation, the energy dispersion of the energy filtered camera will be calibrated by a standard NiO sample. In addition, complimentary atom probe tomography (APT) experiments are planned to study the composition of the nanolamella structure, and the results will be compared with those measured by XEDS and EELS.

6.2 Rotation speed and nanolamella periodicities

By changing the gaseous supply of the precursors $TiCl_4$ and $AlCl_3$, TiAlN nanolamella coatings with different periodicities can be synthesized. Another planned project is therefore to find out the correlation between the nanolamella periodicity, the gas supply, and the coating growth rate. In addition, the Ti(Al)N/Al(Ti)N interfacial lattice straining pattern may be varied through tuning the nanolamella periodicity. This may in turn influence the thermal instability and the mechanical performance of the coatings, which also can be investigated, if time permits, in this PhD project.

7 References

[1] I. El Azhari, J. Barrirero, J. García, F. Soldera, L. Llanes, F. Mücklich, Atom Probe Tomography investigations on grain boundary segregation in polycrystalline Ti(C,N) and Zr(C,N) CVD coatings, Scr. Mater. 162 (2019) 335–340.

[2] J.J. Gracio, Q.H. Fan, J.C. Madaleno, Diamond growth by chemical vapour deposition, J. Phys. D. Appl. Phys. 43 (2010) 374017.

[3] J. Sheikh-Ahmad, J.P. Davim, Tool wear in machining processes for composites, in: Machining technology for composite materials - Principles and Practice, Woodhead Publishing Limited, Cambridge, 2012: pp. 116–153.

[4] S. Canovic, B. Ljungberg, C. Björmander, M. Halvarsson, CVD TiC/alumina and TiN/alumina multilayer coatings grown on sapphire single crystals, Int. J. Refract. Met. Hard Mater. 28 (2010) 163–173.

[5] M.H. Staia, E.S. Puchi, D.B. Lewis, J. Cawley, D. Morel, Microstructural characterization of chemically vapor deposited TiN coating, Surf. Coatings Technol. 86–87 (1996) 432–437.

[6] L. von Fieandt, K. Johansson, T. Larsson, M. Boman, E. Lindahl, On the growth, orientation and hardness of chemical vapor deposited Ti(C,N), Thin Solid Films. 645 (2018) 19–26.

[7] J. Zalesak, D. Holec, I. Matko, M. Petrenec, B. Sartory, N. Koutná, R. Daniel, R. Pitonak, J. Keckes, Peculiarity of self-assembled cubic nanolamellae in the TiN/AlN system: Epitaxial self-stabilization by element deficiency/excess, Acta Mater. 131 (2017) 391–399.

[8] I. Yonenaga, A. Nikolaev, Y. Melnik, V. Dmitriev, High-Temperature Hardness of Bulk Single-Crystal AlN, Jpn. J. Appl. Phys. 40 (2001) L426–L427.

[9] X.H. Ji, S.P. Lau, G.Q. Yu, W.H. Zhong, B.K. Tay, Structural properties and nanoindentation of AlN films by a filtered cathodic vacuum arc at low temperature, J. Phys. D. Appl. Phys. 37 (2004) 1472–1477.

[10] M. Lee, High temperature hardness of tungsten carbide, Metall. Trans. A. 14 (1983) 1625–1629.

[11] C.P. Alpert, H.M. Chan, S.J. Bennison, B. Lawn, Temperature Dependence of Hardness of Alumina-Based Ceramics, J. Am. Ceram. Soc. 71 (1988) C-371-C-373.

[12] S. PalDey, S.C. Deevi, Single layer and multilayer wear resistant coatings of (Ti,Al)N: a review, Mater. Sci. Eng. A. 342 (2003) 58–79.

[13] D.-Y. Wang, C.-L. Chang, K.-W. Wong, Y.-W. Li, W.-Y. Ho, Improvement of the interfacial integrity of (Ti,Al)N hard coatings deposited on high speed steel cutting tools, Surf. Coatings Technol. 120–121 (1999) 388–394.

[14] X. Jiang, J. Philip, W.J. Zhang, P. Hess, S. Matsumoto, Hardness and Young's modulus of high-quality cubic boron nitride films grown by chemical vapor deposition, J. Appl. Phys. 93 (2003) 1515–1519.

[15] W.A. Bryant, The fundamentals of chemical vapour deposition, J. Mater. Sci. 12 (1977) 1285–1306.

[16] J. -E. Sundgren, H.T.G. Hentzell, A review of the present state of art in hard coatings grown from the vapor phase, J. Vac. Sci. Technol. A. 4 (1986) 2259–2279.

[17] U. König, R. Tabersky, H. van den Berg, Research, development and performance of cemented carbide tools coated by plasma-activated chemical vapour deposition, Surf. Coatings Technol. 50 (1991) 57–62.

[18] D.T. Quinto, A.T. Santhanam, P.C. Jindal, Mechanical properties, structure and performance of chemically vapor-deposited and physically vapor-deposited coated carbide tools, Mater. Sci. Eng. A. 105–106 (1988) 443–452.

[19] H.E. Hintermann, Tribological and protective coatings by chemical vapour deposition, Thin Solid Films. 84 (1981) 215–243.

[20] K.-H. Habig, G.M. zu Köcker, Possibilities of model wear testing for the preselection of hard coatings for cutting tools, Surf. Coatings Technol. 62 (1993) 428–437.

[21] W. Schintlmeister, O. Pacher, Preparation and properties of hard-material layers for

metal machining and jewelry, J. Vac. Sci. Technol. 12 (1975) 743–748.

[22] J.P. Chubb, J. Billingham, D.D. Hall, J.M. Walls, Comparison of wear behaviour of single- and multilayer coated carbide cutting tools, Met. Technol. 7 (1980) 293–299.

[23] K.K. Yee, Protective coatings for metals by chemical vapour deposition, Int. Met. Rev. 23 (1978) 19–42.

[24] B. Lux, R. Haubner, C. Wohlrab, Chemically vapour-deposited hard coatings: Applications and selection guidelines, Surf. Coatings Technol. 38 (1989) 267–280.

[25] H.O. Pierson, Handbook of Chemical Vapour Deposition (CVD) - Principles, Technology, and Applications, Elsevier, Norwich, NY, 1999.

[26] L. von Fieandt, Cutting edge titanium-based CVD hard coatings, PhD thesis, Uppsala University, 2018.

[27] M.C.V. Y. Hamedani, P. Macha, T. J. Bunning, R. R. Naik, Plasma-enhanced chemical vapor deposition: Where we are and the outlook for the future, Chem. Vap. Depos. Adv. Appl. Opt. Sol. Cells Solid State Devices, InTech. (2016).

[28] A. Kar, J. Mazumder, Laser chemical vapor deposition of thin films, Mater. Sci. Eng. B. 41 (1996) 368–373.

[29] J.-O. Carlsson, U. Jansson, Progress in chemical vapor deposition, Prog. Solid State Chem. 22 (1993) 237–292.

[30] B.E. Deal, A.S. Grove, General Relationship for the Thermal Oxidation of Silicon, J. Appl. Phys. 36 (1965) 3770–3778.

[31] Y. Song, S. Dhar, L.C. Feldman, G. Chung, J.R. Williams, Modified Deal Grove model for the thermal oxidation of silicon carbide, J. Appl. Phys. 95 (2004) 4953–4957.

[32] M. Rieutord, Fluid dynamics - An introduction, Springer International Publishing, Cham, 2015.

[33] A. Sherman, Growth and Properties of LPCVD Titanium Nitride as a Diffusion Barrier for Silicon Device Technology, J. Electrochem. Soc. 137 (1990) 1892/1897.

[34] H. Holleck, Material selection for hard coatings, J. Vac. Sci. Technol. A. 4 (1986) 2661–2669.

[35] S. Schiller, G. Beister, J. Reschke, G. Hoetzsch, TiN hard coatings deposited on high-speed steel substrates by reactive direct current magnetron sputtering, J. Vac. Sci. Technol. A Vacuum, Surfaces, Film. 5 (1987) 2180–2183.

[36] M. Griepentrog, B. Mackrodt, G. Mark, T. Linz, Properties of TiN hard coatings prepared by unbalanced magnetron sputtering and cathodic arc deposition using a uni- and bipolar pulsed bias voltage, Surf. Coatings Technol. 74–75 (1995) 326–332.

[37] L. von Fieandt, T. Larsson, E. Lindahl, O. Bäcke, M. Boman, Chemical vapor deposition of TiN on transition metal substrates, Surf. Coatings Technol. 334 (2018) 373–383.

[38] I. Endler, M. Höhn, M. Herrmann, R. Pitonak, S. Ruppi, M. Schneider, H. van den Berg, H. Westphal, Novel aluminum-rich $Ti_{1-x}Al_xN$ coatings by LPCVD, Surf. Coatings Technol. 203 (2008) 530–533.

[39] A. Kimura, H. Hasegawa, K. Yamada, T. Suzuki, Metastable $Ti_{1-x}Al_xN$ films with different Al content, J. Mater. Sci. Lett. 19 (2000) 601–602.

[40] M. Zhou, Y. Makino, M. Nose, K. Nogi, Phase transition and properties of Ti–Al–N thin films prepared by r.f.-plasma assisted magnetron sputtering, Thin Solid Films. 339 (1999) 203–208.

[41] A. Hörling, L. Hultman, M. Odén, J. Sjölén, L. Karlsson, Thermal stability of arc evaporated high aluminum-content $Ti_{1-x}Al_xN$ thin films, J. Vac. Sci. Technol. A. 20 (2002) 1815–1823.

[42] P.H. Mayrhofer, A. Hörling, L. Karlsson, J. Sjölén, T. Larsson, C. Mitterer, L. Hultman, Self-organized nanostructures in the Ti–Al–N system, Appl. Phys. Lett. 83 (2003) 2049–2051.

[43] J. Todt, J. Zalesak, R. Daniel, R. Pitonak, A. Köpf, R. Weißenbacher, B. Sartory, C. Mitterer, J. Keckes, Al-rich cubic $Al_{0.8}Ti_{0.2}N$ coating with self-organized nano-lamellar microstructure: Thermal and mechanical properties, Surf. Coatings Technol. 291 (2016) 89–93.

[44] A. Paseuth, K. Yamagata, A. Miura, M. Higuchi, K. Tadanaga, M. Cinibulk, Deposition and Analysis of Al-Rich c-$Al_xTi_{1-x}N$ Coating with Preferred Orientation, J. Am. Ceram. Soc. 100 (2016) 343–353.

[45] K. Bartsch, A. Leonhardt, E. Wolf, Deposition of multilayer hard coatings using kinetically controlled chemical vapour deposition processes, Surf. Coatings Technol. 54–55 (1992) 193–197.

[46] J. Keckes, R. Daniel, C. Mitterer, I. Matko, B. Sartory, A. Koepf, R. Weißenbacher, R. Pitonak, Self-organized periodic soft-hard nanolamellae in polycrystalline TiAlN thin films, Thin Solid Films. 545 (2013) 29–32.

[47] J. Todt, R. Pitonak, A. Köpf, R. Weißenbacher, B. Sartory, M. Burghammer, R. Daniel, T. Schöberl, J. Keckes, Superior oxidation resistance, mechanical properties and residual stresses of an Al-rich nanolamellar $Ti_{0.05}Al_{0.95}N$ coating prepared by CVD, Surf. Coatings Technol. 258 (2014) 1119–1127.

[48] Q. Guo, A. Yoshida, Temperature Dependence of Band Gap Change in InN and AlN, Jpn. J. Appl. Phys. 33 (1994) 2453–2456.

[49] D.W. Palmer, 4.12 - Electronic Energy Levels in Group-III Nitrides, in: P. Bhattacharya, R. Fornari, H.Kamimura (Eds.), Comprehensive Semiconductor Science and Technology, Elsevier, Amsterdam, 2011: pp. 390–447.

[50] A. Elshabini, F. Barlow, Semiconductor Packages, in: K.H.J. Buschow, R.W. Cahn, M.C. Flemings, B. Ilschner, E.J. Kramer, S. Mahajan, Encyclopedia of Materials: Science and Technology (Eds.), Elsevier, Amsterdam, 2001: pp. 8339–8356.

[51] U. Wahlström, L. Hultman, J.E. Sundgren, F. Adibi, I. Petrov, J.E. Greene, Crystal growth and microstructure of polycrystalline $Ti_{1-x}Al_xN$ alloy films deposited by ultra-high-vacuum dual-target magnetron sputtering, Thin Solid Films. 235 (1993) 62–70.

[52] Introduction to X-ray Powder Diffractometry, in: Introd. to X-Ray Powder Diffractometry, John Wiley & Sons, Inc., Hoboken, NJ, USA, 2012.

[53] H.-R. Wenk, P. Van Houtte, Texture and anisotropy, Reports Prog. Phys. 67 (2004) 1367–1428.

[54] Y. Homma, S. Suzuki, Y. Kobayashi, M. Nagase, D. Takagi, Mechanism of bright selective imaging of single-walled carbon nanotubes on insulators by scanning electron microscopy, Appl. Phys. Lett. 84 (2004) 1750–1752.

[55] D.B. Williams, C.B. Carter, Transmission Electron Microscopy: A Textbook for Materials Science, Springer US, Boston, MA, 2009.

[56] R. Erni, Aberration-Corrected Imaging in Transmission Electron Microscopy - An introduction, World Scientific Publishing, Singapore, 2015.

[57] R.F. Egerton, Electron energy-loss spectroscopy in the TEM, Reports Prog. Phys. 72 (2009) 16502.

[58] H. Inada, L. Wu, J. Wall, D. Su, Y. Zhu, Performance and image analysis of the aberration-corrected Hitachi HD-2700C STEM, Microscopy. 58 (2009) 111–122.

[59] P. Hartel, H. Rose, C. Dinges, Conditions and reasons for incoherent imaging in STEM, Ultramicroscopy. 63 (1996) 93–114.

[60] F.A. Stevie, L.A. Giannuzzi, B.I. Prenitzer, The Focused Ion Beam Instrument, in: L.A. Giannuzzi, F.A. Stevie (Eds.), Introd. to Focus. Ion Beams, Springer US, Boston, MA, 2005: pp. 1–12.

[61] D. Tomus, H.P. Ng, In situ lift-out dedicated techniques using FIB–SEM system for TEM specimen preparation, Micron. 44 (2013) 115–119.

[62] M. Schaffer, B. Schaffer, Q. Ramasse, Sample preparation for atomic-resolution STEM at low voltages by FIB, Ultramicroscopy. 114 (2012) 62–71.

[63] R.A. Schwarzer, D.P. Field, B.L. Adams, M. Kumar, A.J. Schwartz, Present State of Electron Backscatter Diffraction and Prospective Developments, in: Electron Backscatter Diffraction in Materials Science, Springer US, Boston, MA, 2009.

[64] R.R. Keller, R.H. Geiss, Transmission EBSD from 10 nm domains in a scanning electron microscope, J. Microsc. 245 (2012) 245–251.

[65] A. Sobachkin, G. Dumnov, Numerical Basis of CAD-Embedded CFD, in: Proc. NAFEMS World Congr., 2013.

[66] G. Velo, A.S. Wightman, Rigorous Atomic and Molecular Physics, US, Springer, Boston, MA, 1981.

[67] V. Sahni, Quantal Density Functional Theory, Springer Berlin Heidelberg, Berlin, Heidelberg, 2004.

[68] G. Kresse, J. Furthmüller, Efficient iterative schemes for ab initio total-energy calculations using a plane-wave basis set, Phys. Rev. B. 54 (1996) 11169–11186.

[69] H. Lukas, S.G. Fries, B. Sundman, Computational Thermodynamics: The Calphad Method, Cambridge University Press, Cambridge, 2007.

[70] J.-O. Andersson, T. Helander, L. Höglund, P. Shi, B. Sundman, Thermo-Calc & DICTRA, computational tools for materials science, Calphad. 26 (2002) 273–312.

[71] M. Pons, R. Boichot, N. Coudurier, A. Claudel, E. Blanquet, S. Lay, F. Mercier, D. Pique, High temperature chemical vapor deposition of aluminum nitride, growth and evaluation, Surf. Coatings Technol. 230 (2013) 111–118.

[72] C. Pozrikidis, Fluid Dynamics: Theory, Computation, and Numerical Simulation, Springer US, Boston, MA, 2001.